Received: 11 November 2025 | Revised: 9 May 2026 | Accepted: 22 May 2026

DOI: 10.1002/gamm.70014

ORIGINAL ARTICLE

Local continuum consistent peridynamics with bond-associated modeling and dynamic fracture

Kai Partmann[1] | **Robert I. Weinbrenner**[1] | **Christian Wieners**[2] | **Kerstin Weinberg**[1]

[1]Chair of Solid Mechanics, University of Siegen, Siegen, Germany

[2]Institute of Applied and Numerical Mathematics, Karlsruhe Institute of Technology, Karlsruhe, Germany

Correspondence
Kai Partmann, Chair of Solid Mechanics, University of Siegen, Paul-Bonatz-Str. 9-11, Siegen 57076, Germany.
Email: kai.partmann@uni-siegen.de

Funding information
Deutsche Forschungsgemeinschaft, Grant/Award Number: 422730790

Abstract

This paper explores the theoretical foundations and practical challenges of peridynamics as a nonlocal continuum mechanics method. We establish connections between classical continuum mechanics principles and peridynamics formulations, with a particular focus on understanding how the pairwise force function in peridynamics relates to stress concepts in local theories. The work addresses persistent numerical challenges in peridynamic simulations, including zero-energy modes and instabilities in correspondence-based formulations. We present bond-associated modeling approaches that enhance stability while maintaining computational accuracy. The theoretical discussions are supplemented with discretization methods for spatial and temporal domains. Through illustrative examples of complex fracture phenomena, we demonstrate how these theoretical insights translate to practical applications, providing guidance on selecting appropriate peridynamic formulations for computational mechanics problems. The numerical comparison identifies the bond-associated quadrature point formulation as the most accurate correspondence-class approach in the elastic regime. Under progressive bond deletion, however, the shape tensor, on which this formulation relies, becomes ill-conditioned, and the model loses stability. This necessitates the development of refined damage formulations within the correspondence framework.

KEYWORDS

dynamic fracture, nonlocal models, peridynamics

1 | INTRODUCTION

Peridynamics is a nonlocal continuum mechanics theory that addresses fundamental challenges in the modeling of material discontinuities such as fractures and cracks [33, 34]. Unlike classical continuum mechanics, which relies on partial differential equations that assume spatial differentiability of the displacement field, peridynamics employs integro-differential equations that remain solvable in the presence of discontinuities [35]. The fundamental concept of peridynamics is the interaction between material points through bonds within a finite horizon. This nonlocal interaction replaces the local notion of stress and naturally captures crack initiation, branching, and coalescence without requiring special numerical treatment or predefined crack paths. This makes the theory particularly suitable for dynamic fracture problems [11, 27].

Over the years, peridynamics has evolved from its original bond-based formulation, which is limited by a fixed Poisson's ratio [36], to more general frameworks. State-based peridynamics [35] and the correspondence formulation [25] extend the theory to general constitutive laws, but they introduce numerical instabilities such as zero-energy modes [7]. A range of stabilization techniques and bond-associated modeling approaches has been proposed to address these issues. Among them are continuum-kinematics-inspired peridynamics [19, 20], the bond-associated subdomain of Chen and Spencer [7], and the bond-associated quadrature point formulation [1]. These approaches aim to retain the flexibility of the correspondence formulation while improving accuracy and stability through stronger ties to classical continuum mechanics.

The present work focuses on the theoretical and practical comparison of these formulations. We revisit the connection between local and nonlocal continuum theories, examine the objectivity enforcement technique under large smooth deformations, and assess the stability of the correspondence formulation through three numerical tests. A three-dimensional checkerboard patch test exposes how zero-energy modes manifest in correspondence-class models. A traction-load study quantifies the elastic response and the well-known surface effect [22]. A mode I crack and a dynamic crack branching benchmark probe the behavior under fracture. The comparison shows that the bond-associated quadrature point formulation is the most accurate correspondence-class formulation in the elastic regime, but it also reveals a clear limitation of this formulation under progressive bond deletion. We discuss this limitation, identify its origin in the construction of the bond-associated deformation gradient, and outline the regime in which each formulation can be applied with confidence.

This paper is organized as follows. Section 2 reviews the fundamentals of local continuum mechanics. Section 3 introduces peridynamics as a nonlocal continuum theory, presents the spatial discretization, and describes both the explicit Velocity-Verlet scheme and the implicit Jacobian-free Newton–Krylov solver used in this work. Section 4 discusses zero-energy modes and bond-associated modeling approaches, including the three-dimensional patch test and the large-deformation analysis of objectivity enforcement. Section 5 presents numerical results comparing the formulations on a traction-load convergence study, a mode I crack, and the dynamic crack branching benchmark. Section 6 provides conclusions and outlook.

2 | FUNDAMENTALS OF CONTINUUM MECHANICS

In the following, the fundamentals of continuum mechanics are briefly summarized. Although these fundamentals are well known to the reader, they are necessary to understand the similarities and differences between classical continuum mechanics and peridynamics. The focus is on the description of the motion of a continuum body, the deformation gradient, and the strain measures. These concepts are later used to derive the peridynamics equations and to establish the connection to the local continuum theory.

2.1 | Configurations as motion of continuum bodies

A body $\mathcal{B}$ can be considered a continuum with infinite material points in Euclidean space $\mathbb{R}^3$. The configuration of body $\mathcal{B}$ is described as a reversible, unique mapping of all material points to the points of the space with the help of a location vector or a coordinate system. Specifically, the bijective mapping

$$\boldsymbol{\Phi}_t : \mathcal{B}_0 \to \mathcal{B}_t \qquad \exists\, \boldsymbol{\Phi}_t^{-1} : \mathcal{B}_t \to \mathcal{B}_0 \tag{2.1}$$

describes the transformation (deformation) of the body from reference configuration $\mathcal{B}_0$ to current configuration $\mathcal{B}_t$ for the time t. The movement of a body can therefore be described as a parametrical (temporal) sequence of deformations $\boldsymbol{\Phi} : [0, \infty) \times \mathcal{B} \to \mathbb{R}^3$ with $\boldsymbol{\Phi}(t, \boldsymbol{X}) = \boldsymbol{\Phi}_t(\boldsymbol{X})$.

As displayed in Figure 1, the initial position of a material point in the reference configuration is described as $\boldsymbol{X}$. With the transformation $\boldsymbol{\Phi}$, the position of a point at time t is defined as

$$\boldsymbol{x}(t, \boldsymbol{X}) = \boldsymbol{\Phi}(t, \boldsymbol{X}) \qquad \forall \boldsymbol{X} \in \mathcal{B}_0. \tag{2.2}$$

For convenience, the notation $\boldsymbol{x} = \boldsymbol{x}(t, \boldsymbol{X})$ is also used in the following. Every point $\boldsymbol{x}$ can be uniquely mapped back to the reference configuration

$$\boldsymbol{X} = \boldsymbol{\Phi}^{-1}(t, \boldsymbol{x}) \qquad \forall \boldsymbol{x} \in \mathcal{B}_t, \tag{2.3}$$

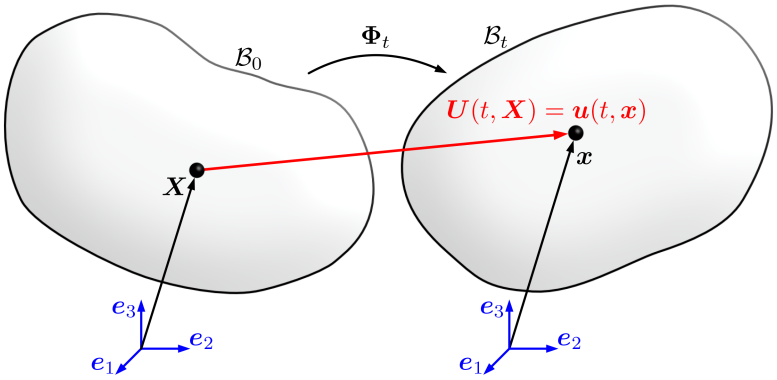

FIGURE 1 Deformation of a body $\mathcal{B}$ from reference configuration $\mathcal{B}_0$ to current configuration $\mathcal{B}_t$.

since $\boldsymbol{\Phi}$ is bijective and the inversion $\boldsymbol{\Phi}^{-1}$ exists. The initial position $\boldsymbol{X}$ is also called the material coordinate; the current position $\boldsymbol{x}$ is also called spatial coordinate.

The so-called *material* description is a characterization of the motion (or any other quantity) with respect to the reference coordinates $\boldsymbol{X}$ and time t, described by Equation (2.2). Traditionally, the material description is often referred to as the *Lagrangian* description. At $t = 0$, there is the consistency condition $\boldsymbol{X} = \boldsymbol{x}$. With the geometric difference between the initial and current position, the material displacement field $\boldsymbol{U}$ is defined as

$$\boldsymbol{U}(t, \boldsymbol{X}) = \boldsymbol{\Phi}(t, \boldsymbol{X}) - \boldsymbol{X} = \boldsymbol{x} - \boldsymbol{X}. \tag{2.4}$$

This Lagrangian description is based on the idea of following the motion of a material point from its initial position $\boldsymbol{X}$ to its current position $\boldsymbol{x}$ through space. Because attention is paid to a specific point, it is observed what happens to the material as it moves through space.

On the other hand, the so-called *spatial* description is a characterization of the motion (or any other quantity) with respect to the spatial coordinates $\boldsymbol{x}$ and time t, given by Equation (2.3). The spatial description is often also referred to as the *Eulerian* description. In contrast to the Lagrangian description, the Eulerian description is based on the idea of observing the motion of a material point at a fixed spatial position $\boldsymbol{x}$. The spatial displacement field $\boldsymbol{u}$ in Eulerian description is defined as

$$\boldsymbol{u}(t, \boldsymbol{x}) = \boldsymbol{x} - \boldsymbol{\Phi}^{-1}(t, \boldsymbol{x}) = \boldsymbol{x} - \boldsymbol{X}. \tag{2.5}$$

Because attention is paid to a specific point in space, the observation is made from a spatial or Eulerian point of view. The value and direction of the material and spatial displacement fields are identical,

$$\boldsymbol{U}(t, \boldsymbol{X}) = \boldsymbol{U}\left(t, \boldsymbol{\Phi}^{-1}(t, \boldsymbol{x})\right) = \boldsymbol{u}(t, \boldsymbol{x}), \tag{2.6}$$

the main difference is just their relation to $\boldsymbol{X}$ or $\boldsymbol{x}$, respectively.

The velocity of a material point $\boldsymbol{X}$ in the material description is with Equation (2.4) defined as

$$\dot{\boldsymbol{U}}(t, \boldsymbol{X}) = \frac{\partial \boldsymbol{U}(t, \boldsymbol{X})}{\partial t} = \frac{\partial \boldsymbol{\Phi}(t, \boldsymbol{X})}{\partial t}, \tag{2.7}$$

with $\partial \boldsymbol{X}/\partial t = 0$. The material velocity field $\dot{\boldsymbol{U}}$ is also referred to as the instantaneous velocity field. Analogously, the material acceleration field or instantaneous acceleration $\ddot{\boldsymbol{U}}$ is defined as

$$\ddot{\boldsymbol{U}}(t, \boldsymbol{X}) = \frac{\partial \dot{\boldsymbol{U}}(t, \boldsymbol{X})}{\partial t} = \frac{\partial^2 \boldsymbol{\Phi}(t, \boldsymbol{X})}{\partial t^2}. \tag{2.8}$$

In contrast, the velocity at a spatial position $\boldsymbol{x}$ and time t is described by the (identical) spatial velocity field

$$\dot{\boldsymbol{u}}(t, \boldsymbol{x}) = \dot{\boldsymbol{U}}(t, \boldsymbol{\Phi}^{-1}(t, \boldsymbol{x})) = \frac{\partial \boldsymbol{\Phi}\left(t, \boldsymbol{\Phi}^{-1}(t, \boldsymbol{x})\right)}{\partial t}. \tag{2.9}$$

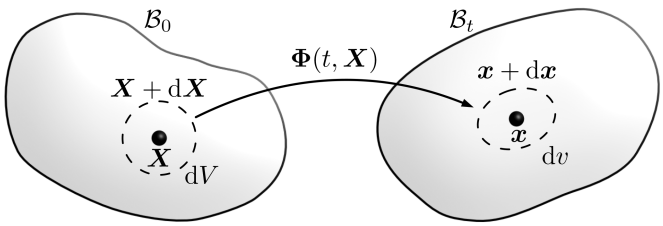

FIGURE 2 Local deformation in the surrounding $\boldsymbol{X} + \mathrm{d}\boldsymbol{X}$ of a material point $\boldsymbol{X}$.

Similarly, the spatial acceleration field $\ddot{\boldsymbol{u}}$ is defined as

$$\ddot{\boldsymbol{u}}(t, \boldsymbol{x}) = \frac{\partial \dot{\boldsymbol{u}}(t, \boldsymbol{x})}{\partial t} = \frac{\partial^2 \boldsymbol{\Phi}\left(t, \boldsymbol{\Phi}^{-1}(t, \boldsymbol{x})\right)}{\partial t^2}. \tag{2.10}$$

2.2 | Local deformations and strain measures

A body deforms when moving from reference configuration $\mathcal{B}_0$ to current configuration $\mathcal{B}_t$. To characterize this deformation, it is necessary to take the infinitesimal surrounding of a material point into consideration. Let $\mathrm{d}V \subset \mathcal{B}_0$ be the volume of an infinitesimal material neighborhood of point $\boldsymbol{X} \in \mathcal{B}_0$ in the reference configuration. Accordingly, the volume $\mathrm{d}v$ describes the infinitesimal volume of the same material neighborhood in the current configuration, as displayed in Figure 2. If we consider a neighboring point $\boldsymbol{X} + \mathrm{d}\boldsymbol{X}$ with $\mathrm{d}\boldsymbol{X} \in \mathbb{R}^3$ inside any volume $\mathrm{d}V$, the corresponding point $\boldsymbol{x} + \mathrm{d}\boldsymbol{x}$ in the current configuration yields

$$\boldsymbol{x} + \mathrm{d}\boldsymbol{x} = \boldsymbol{\Phi}(t, \boldsymbol{X} + \mathrm{d}\boldsymbol{X}). \tag{2.11}$$

The motion of the surrounding $\boldsymbol{\Phi}(t, \boldsymbol{X} + \mathrm{d}\boldsymbol{X})$ can be expanded in a Taylor series at position $\boldsymbol{X}$, leading to

$$\boldsymbol{\Phi}(t, \boldsymbol{X} + \mathrm{d}\boldsymbol{X}) = \boldsymbol{\Phi}(t, \boldsymbol{X}) + \frac{\partial \boldsymbol{\Phi}(t, \boldsymbol{X})}{\partial \boldsymbol{X}}\, \mathrm{d}\boldsymbol{X} + \mathcal{O}(|\mathrm{d}\boldsymbol{X}|^2), \tag{2.12}$$

where the higher-order terms $\mathcal{O}(|\mathrm{d}\boldsymbol{X}|^2)$ are negligible for infinitesimally small $\mathrm{d}\boldsymbol{X}$ and

$$\lim_{|\mathrm{d}\boldsymbol{X}| \to 0} \boldsymbol{\Phi}(t, \boldsymbol{X} + \mathrm{d}\boldsymbol{X}) = \boldsymbol{x}, \tag{2.13}$$

recovering Equation (2.2). Transformation with Equation (2.2) yields

$$\mathrm{d}\boldsymbol{x} = \boldsymbol{\Phi}(t, \boldsymbol{X} + \mathrm{d}\boldsymbol{X}) - \boldsymbol{\Phi}(t, \boldsymbol{X}) = \frac{\partial \boldsymbol{\Phi}(t, \boldsymbol{X})}{\partial \boldsymbol{X}}\, \mathrm{d}\boldsymbol{X} + \mathcal{O}(|\mathrm{d}\boldsymbol{X}|^2). \tag{2.14}$$

Neglecting the terms $\mathcal{O}(|\mathrm{d}\boldsymbol{X}|^2)$, we obtain the linearized differential relation

$$\mathrm{d}\boldsymbol{x} = \frac{\partial \boldsymbol{\Phi}(t, \boldsymbol{X})}{\partial \boldsymbol{X}}\, \mathrm{d}\boldsymbol{X}. \tag{2.15}$$

With Equation (2.15), the deformation gradient $\boldsymbol{F} : [0, \infty) \times \mathcal{B} \to \mathbb{R}^{3\times3}$ is defined as second order tensor

$$\boldsymbol{F}(t, \boldsymbol{X}) = \frac{\partial \boldsymbol{\Phi}(t, \boldsymbol{X})}{\partial \boldsymbol{X}} = \frac{\mathrm{d}\boldsymbol{x}}{\mathrm{d}\boldsymbol{X}}. \tag{2.16}$$

The deformation gradient $\boldsymbol{F}$ is fundamental in nonlinear continuum mechanics and is the primary measure of deformation. It characterizes the behavior of motion at time t in the infinitesimal material neighborhood $\mathrm{d}\boldsymbol{X}$ of $\boldsymbol{X}$. With Equation (2.4), the deformation gradient $\boldsymbol{F}$ can be written as

$$\boldsymbol{F}(t, \boldsymbol{X}) = \frac{\partial \boldsymbol{\Phi}(t, \boldsymbol{X})}{\partial \boldsymbol{X}} = \boldsymbol{I} + \frac{\partial \boldsymbol{U}(t, \boldsymbol{X})}{\partial \boldsymbol{X}} = \boldsymbol{I} + \nabla \boldsymbol{U}(t, \boldsymbol{X}), \tag{2.17}$$

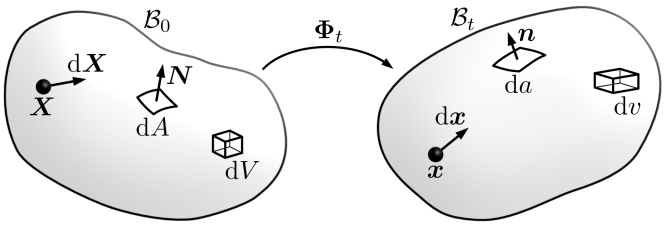

FIGURE 3 Line-, surface-, and volume elements in reference and current configuration.

with the displacement gradient

$$\nabla \boldsymbol{U}(t,\boldsymbol{X}) = \frac{\partial \boldsymbol{U}(t,\boldsymbol{X})}{\partial \boldsymbol{X}}. \tag{2.18}$$

Utilizing the inverse deformation $\boldsymbol{\Phi}^{-1}(t,\boldsymbol{x})$, the inversion of the deformation gradient $\boldsymbol{F}$ yields

$$\boldsymbol{F}^{-1}(t,\boldsymbol{x}) = \frac{\partial \boldsymbol{\Phi}^{-1}(t,\boldsymbol{x})}{\partial \boldsymbol{x}} = \frac{\mathrm{d}\boldsymbol{X}}{\mathrm{d}\boldsymbol{x}}. \tag{2.19}$$

The inverse deformation gradient $\boldsymbol{F}^{-1}$ maps $\mathrm{d}\boldsymbol{x}$ to $\mathrm{d}\boldsymbol{X}$ with $\mathrm{d}\boldsymbol{X} = \boldsymbol{F}^{-1}(t,\boldsymbol{x})\,\mathrm{d}\boldsymbol{x}$. Generally, the deformation gradient is nonsingular and invertible, which consequently results in the condition $\det \boldsymbol{F} \neq 0$.

From Equation (2.16), it clearly follows with

$$\mathrm{d}\boldsymbol{x} = \boldsymbol{F}(t,\boldsymbol{X})\,\mathrm{d}\boldsymbol{X}, \tag{2.20}$$

that the deformation gradient is a linear transformation of the *material line element* $\mathrm{d}\boldsymbol{X}$ from the reference configuration to $\mathrm{d}\boldsymbol{x}$ in the current configuration, as displayed in Figure 3.

The determinant of the deformation gradient $\boldsymbol{F}$ is defined as the Jacobian

$$J(t,\boldsymbol{X}) = \det \boldsymbol{F}(t,\boldsymbol{X}). \tag{2.21}$$

From the invertibility of $\boldsymbol{F}$ it follows that $J(t,\boldsymbol{X}) \neq 0$. Because volume elements cannot have negative volumes and matter cannot overlap, we obtain the condition

$$J(t,\boldsymbol{X}) > 0 \qquad \forall (t,\boldsymbol{X}) \in [0,\infty) \times \mathcal{B}_0. \tag{2.22}$$

Considering the *material volume element* $\mathrm{d}V \subset \mathcal{B}_0$ of the infinitesimal neighborhood $\boldsymbol{X} + \mathrm{d}\boldsymbol{X}$ as the parallelepipedic product

$$\mathrm{d}V = (\mathrm{d}\boldsymbol{X}_1 \times \mathrm{d}\boldsymbol{X}_2) \cdot \mathrm{d}\boldsymbol{X}_3, \tag{2.23}$$

with $\mathrm{d}\boldsymbol{X} = \mathrm{d}\boldsymbol{X}_1\,\mathrm{d}\boldsymbol{X}_2\,\mathrm{d}\boldsymbol{X}_3$, the volume element $\mathrm{d}v \subset \mathcal{B}_t$ in the current configuration is given by

$$\mathrm{d}v = (\mathrm{d}\boldsymbol{x}_1 \times \mathrm{d}\boldsymbol{x}_2) \cdot \mathrm{d}\boldsymbol{x}_3 = \det \boldsymbol{F}[(\mathrm{d}\boldsymbol{X}_1 \times \mathrm{d}\boldsymbol{X}_2) \cdot \mathrm{d}\boldsymbol{X}_3] = J\,\mathrm{d}V, \tag{2.24}$$

with $\mathrm{d}\boldsymbol{x}_i = \boldsymbol{F}\,\mathrm{d}\boldsymbol{X}_i$ for $i \in \{1,2,3\}$. Consequently, the Jacobian can be defined as the ratio of the current volume to the reference volume

$$J(t,\boldsymbol{X}) = \frac{\mathrm{d}v}{\mathrm{d}V}. \tag{2.25}$$

Evidently, the Jacobian J is a measure of the local volume change of the body. If there is no motion, the Jacobian yields $J = \det \boldsymbol{I} = 1$. A motion or deformation with a Jacobian of $J = 1$ is volume-preserving and called isochoric.

Let the boundary of the reference configuration $\mathcal{B}_0$ be denoted by $\partial\mathcal{B}_0$, and the boundary of the current configuration $\mathcal{B}_t$ be denoted by $\partial\mathcal{B}_t$. To find a relation between the oriented *material surface element* $\mathrm{d}A \subset \partial\mathcal{B}_0$ and $\mathrm{d}a \subset \partial\mathcal{B}_t$, the normal vectors $\boldsymbol{N}$ and $\boldsymbol{n}$ need to be considered with

$$\mathrm{d}V = \mathrm{d}\boldsymbol{X} \cdot \boldsymbol{N}\, \mathrm{d}A, \qquad \mathrm{d}v = \mathrm{d}\boldsymbol{x} \cdot \boldsymbol{n}\, \mathrm{d}a. \tag{2.26}$$

Transforming Equation (2.26) with (2.25) and (2.20), the relation between the surface elements yields

$$\mathrm{d}\boldsymbol{X} \cdot \boldsymbol{N}\, \mathrm{d}A = J^{-1}\, \mathrm{d}\boldsymbol{x} \cdot \boldsymbol{n}\, \mathrm{d}a = J^{-1}\boldsymbol{F}\, \mathrm{d}\boldsymbol{X} \cdot \boldsymbol{n}\, \mathrm{d}a = \mathrm{d}\boldsymbol{X} \cdot J^{-1}\boldsymbol{F}^{\top}\boldsymbol{n}\, \mathrm{d}a. \tag{2.27}$$

With a small transformation, omitting $\mathrm{d}\boldsymbol{X}$ in Equation (2.27) gives the relation between the surface elements $\mathrm{d}A$ and $\mathrm{d}a$ as

$$\boldsymbol{n}\, \mathrm{d}a = J\boldsymbol{F}^{-\top}\boldsymbol{N}\, \mathrm{d}A. \tag{2.28}$$

The relationship in Equation (2.28) is also called **Nanson's formula** [18].

There are different strain measures, which can be derived from the deformation gradient $\boldsymbol{F}$. Strain measures are required to be symmetric, as they vanish for rigid body motions. An important strain tensor is the *right Cauchy–Green tensor* $\boldsymbol{C}$, which is defined as the square of the right stretch tensor

$$\boldsymbol{C} = \boldsymbol{F}^{\top}\boldsymbol{F}. \tag{2.29}$$

The right Cauchy–Green tensor $\boldsymbol{C}$ is symmetric and positive definite at each $\boldsymbol{X} \in \mathcal{B}_0$. Note that the inverse of the right Cauchy–Green tensor is given by

$$\boldsymbol{C}^{-1} = \left(\boldsymbol{F}^{\top}\boldsymbol{F}\right)^{-1} = \boldsymbol{F}^{-1}\boldsymbol{F}^{-\top}. \tag{2.30}$$

From Equation (2.29) and (2.21), it follows that

$$\det \boldsymbol{C} = (\det \boldsymbol{F})^2 = J^2 > 0. \tag{2.31}$$

The right Cauchy–Green tensor is a material strain measure, while the left Cauchy–Green tensor $\boldsymbol{b} = \boldsymbol{F}\boldsymbol{F}^{\top}$ is associated with the spatial configuration [18].

The *Green-Lagrange strain tensor* $\boldsymbol{E}$ is defined as

$$\boldsymbol{E} = \frac{1}{2}\left(\boldsymbol{F}^{\top}\boldsymbol{F} - \boldsymbol{I}\right) = \frac{1}{2}(\boldsymbol{C} - \boldsymbol{I}), \tag{2.32}$$

and has the properties $\boldsymbol{E} = \boldsymbol{E}^{\top}$ since $\boldsymbol{C}$ and $\boldsymbol{I}$ are symmetric, and also $\boldsymbol{E} = \boldsymbol{0}$ if and only if $\boldsymbol{F} = \boldsymbol{I}$. Consequently, the Green–Lagrange strain tensor is zero in all components if there is no deformation. The Green–Lagrange strain tensor can also be expressed in terms of the displacement gradient $\nabla\boldsymbol{U}$ with Equation (2.17) as

$$\boldsymbol{E} = \frac{1}{2}\left((\nabla\boldsymbol{U} + \boldsymbol{I})^{\top}(\nabla\boldsymbol{U} + \boldsymbol{I}) - \boldsymbol{I}\right) = \frac{1}{2}\left(\nabla\boldsymbol{U} + \nabla\boldsymbol{U}^{\top} + \nabla\boldsymbol{U}^{\top}\nabla\boldsymbol{U}\right). \tag{2.33}$$

The material response to deformation is often characterized using the bulk modulus K and the shear modulus G. The bulk modulus K describes a material's resistance to uniform compression, while the shear modulus G quantifies its resistance to shear deformation. These moduli are fundamental in constitutive modeling and relate stress to strain in isotropic materials. The bulk modulus K and shear modulus G in three dimensions are related to Young's modulus E and Poisson's ratio ν by

$$K = \frac{E}{3(1-2\nu)}, \qquad G = \frac{E}{2(1+\nu)}. \tag{2.34}$$

In the infinitesimal strain theory, the deformation gradient $\boldsymbol{F}$ is presumed to be close to the identity $\boldsymbol{I}$. Consequently, the reference and current configurations are assumed to be close to each other. This assumption is valid in virtually all solid materials under sufficiently small loading conditions [37]. As a result, strains are small if

$$\|\nabla\boldsymbol{U}\| = \|\boldsymbol{F} - \boldsymbol{I}\| \ll 1, \tag{2.35}$$

so that a linearization of Equation (2.32) approximates the nonlinear strain measures. The *infinitesimal strain tensor* $\boldsymbol{\varepsilon}$ is defined as the symmetric part of the displacement gradient $\nabla \boldsymbol{U}$ and is given by linearization of Equation (2.33) as

$$\boldsymbol{\varepsilon} = \frac{1}{2}\left(\nabla \boldsymbol{U} + \nabla \boldsymbol{U}^{\mathrm{T}}\right), \tag{2.36}$$

neglecting the nonlinear term $\nabla \boldsymbol{U}^{\mathrm{T}}\, \nabla \boldsymbol{U}$. This also implies that $\boldsymbol{\varepsilon} \approx \boldsymbol{E}$. With Equation (2.17), the infinitesimal strain tensor $\boldsymbol{\varepsilon}$ can be rewritten as

$$\boldsymbol{\varepsilon} = \frac{1}{2}\left((\boldsymbol{F} - \boldsymbol{I}) + (\boldsymbol{F} - \boldsymbol{I})^{\mathrm{T}}\right) = \frac{1}{2}\left(\boldsymbol{F} + \boldsymbol{F}^{\mathrm{T}}\right) - \boldsymbol{I}. \tag{2.37}$$

The change in time of strain measures is described by the strain rates. The *material velocity gradient* $\dot{\boldsymbol{F}}$ is defined as the time derivative of the deformation gradient and is, with Equation (2.16), given by

$$\dot{\boldsymbol{F}}(t, \boldsymbol{X}) = \frac{\partial}{\partial t}\left(\frac{\partial \boldsymbol{\Phi}(t, \boldsymbol{X})}{\partial \boldsymbol{X}}\right) = \frac{\partial}{\partial \boldsymbol{X}}\left(\frac{\partial \boldsymbol{\Phi}(t, \boldsymbol{X})}{\partial t}\right) = \frac{\partial \dot{\boldsymbol{U}}(t, \boldsymbol{X})}{\partial \boldsymbol{X}}. \tag{2.38}$$

The material velocity gradient $\dot{\boldsymbol{F}}$ characterizes the rate of change of the deformation gradient $\boldsymbol{F}$ at a material point $\boldsymbol{X}$. Analogously, the *spatial velocity gradient* $\boldsymbol{l}$ is defined as the derivative of the spatial velocity field with respect to spatial coordinates as

$$\boldsymbol{l}(t, \boldsymbol{x}) = \frac{\partial \dot{\boldsymbol{u}}(t, \boldsymbol{x})}{\partial \boldsymbol{x}}. \tag{2.39}$$

The spatial velocity gradient $\boldsymbol{l}$ can be expressed with Equation (2.38), (2.6), and (2.19) as

$$\boldsymbol{l} = \frac{\partial \dot{\boldsymbol{u}}}{\partial \boldsymbol{x}} = \frac{\partial \dot{\boldsymbol{u}}}{\partial \boldsymbol{X}} \frac{\partial \boldsymbol{X}}{\partial \boldsymbol{x}} = \dot{\boldsymbol{F}} \boldsymbol{F}^{-1}. \tag{2.40}$$

The symmetric part of the spatial velocity gradient is also known as the *rate of deformation tensor* $\boldsymbol{d}$ and is defined as

$$\boldsymbol{d} = \frac{1}{2}\left(\boldsymbol{l} + \boldsymbol{l}^{\mathrm{T}}\right) = \frac{1}{2}\left(\dot{\boldsymbol{F}} \boldsymbol{F}^{-1} + \boldsymbol{F}^{-1} \dot{\boldsymbol{F}}^{\mathrm{T}}\right). \tag{2.41}$$

Furthermore, the antisymmetric part of the spatial velocity gradient is the *spin tensor* $\boldsymbol{w}$, given by

$$\boldsymbol{w} = \frac{1}{2}\left(\boldsymbol{l} - \boldsymbol{l}^{\mathrm{T}}\right) = \frac{1}{2}\left(\dot{\boldsymbol{F}} \boldsymbol{F}^{-1} - \boldsymbol{F}^{-1} \dot{\boldsymbol{F}}^{\mathrm{T}}\right). \tag{2.42}$$

2.3 | Body forces and stress tensors

Solid continuum bodies deform and move over a period of time due to externally applied forces and prescribed displacements. The *material body force field* per unit mass $\overline{\boldsymbol{B}} : [0, \infty) \times \mathcal{B} \to \mathbb{R}^3$ describes forces acting on the body due to interaction at a distance, such as gravitational forces. The *spatial body force field* per unit mass $\overline{\boldsymbol{b}} : [0, \infty) \times \boldsymbol{\Phi}_t(\mathcal{B}) \to \mathbb{R}^3$ acts on the deformed configuration $\boldsymbol{\Phi}_t(\mathcal{B})$. For an infinitesimal neighborhood in reference and current configuration, the relation between the material and spatial body force fields is

$$\overline{\boldsymbol{B}}(t, \boldsymbol{X}) = \overline{\boldsymbol{b}}(t, \boldsymbol{x}). \tag{2.43}$$

Cauchy's theorem states that due to external forces, there exists a *spatial force field* per unit area $\bar{\boldsymbol{t}} : [0, \infty) \times \boldsymbol{\Phi}_t(\mathcal{B}_0) \to \mathbb{R}^3$ on every surface $\mathrm{d}a$ with unit normal vector $\boldsymbol{n}(t, \boldsymbol{x})$ of the body $\mathcal{B}_t$. The surface $\mathrm{d}a$ can be either an internal interface between subdomains or an external boundary surface $\mathrm{d}a \subset \partial \mathcal{B}_t$. If the surface coincides with the external boundary of the body, $\bar{\boldsymbol{t}}$ is also called *spatial traction force field*. Similarly, in the reference configuration it is defined as the *material traction force field* per unit area $\overline{\boldsymbol{T}} : [0, \infty) \times \mathcal{B}_0 \to \mathbb{R}^3$, as displayed in Figure 4. With the infinitesimal area elements $\mathrm{d}A$ and $\mathrm{d}a$, the relation between the material and spatial traction force fields is given by

$$\overline{\boldsymbol{T}}(t, \boldsymbol{X})\, \mathrm{d}A = \bar{\boldsymbol{t}}(t, \boldsymbol{x})\, \mathrm{d}a, \tag{2.44}$$

where $\boldsymbol{X} \in \mathcal{B}_0$ and $\boldsymbol{x} \in \mathcal{B}_t$.

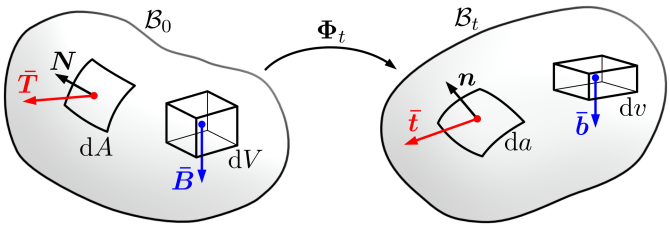

FIGURE 4 Body forces $\bar{\boldsymbol{B}}$, $\bar{\boldsymbol{b}}$ and traction forces $\bar{\boldsymbol{T}}$, $\bar{\boldsymbol{t}}$ in reference and current configuration.

From Cauchy's theorem we know that $\bar{\boldsymbol{t}}$ depends linearly on the normal vector $\boldsymbol{n}$ to the surface element $\mathrm{d}a$ and is given by

$$\bar{\boldsymbol{t}}(t,\boldsymbol{x}) = \boldsymbol{\sigma}(t,\boldsymbol{x})\,\boldsymbol{n}(t,\boldsymbol{x}), \tag{2.45}$$

with the *Cauchy stress tensor* $\boldsymbol{\sigma} : [0,\infty)\times\boldsymbol{\Phi}_t(\mathcal{B}_0) \to \mathbb{R}^{3\times3}$. In a classical Boltzmann continuum, the Cauchy stress tensor $\boldsymbol{\sigma}$ is symmetric at each $\boldsymbol{x}\in\mathcal{B}_t$, therefore

$$\boldsymbol{\sigma} = \boldsymbol{\sigma}^{\mathsf{T}}. \tag{2.46}$$

It is a measure of the true stress at a deformed material point. Equation (2.45) can be written in terms of the reference configuration as

$$\bar{\boldsymbol{T}}(t,\boldsymbol{X}) = \boldsymbol{P}(t,\boldsymbol{X})\,\boldsymbol{N}(t,\boldsymbol{X}), \tag{2.47}$$

with the *first Piola–Kirchhoff stress tensor* $\boldsymbol{P} : [0,\infty)\times\boldsymbol{\Phi}_t(\mathcal{B}_0) \to \mathbb{R}^{3\times3}$.

Inserting Equation (2.45) and (2.47) into (2.44) and using Nanson's formula (2.28) leads to the so-called Piola transformation

$$\boldsymbol{P}(t,\boldsymbol{X}) = J(t,\boldsymbol{X})\,\boldsymbol{\sigma}(t,\boldsymbol{x})\,\boldsymbol{F}^{-\mathsf{T}}(t,\boldsymbol{X}), \tag{2.48}$$

or equivalently

$$\boldsymbol{\sigma}(t,\boldsymbol{x}) = J^{-1}(t,\boldsymbol{X})\,\boldsymbol{P}(t,\boldsymbol{X})\,\boldsymbol{F}^{\mathsf{T}}(t,\boldsymbol{X}). \tag{2.49}$$

The stress tensor $\boldsymbol{P} = \boldsymbol{P}(\boldsymbol{F})$ depends on the deformation and can with the Helmholtz free energy density $\Psi \in C^1(\mathbb{R}^{3\times3})$ be defined as

$$\boldsymbol{P}(\boldsymbol{F}) = \frac{\partial\Psi(\boldsymbol{F})}{\partial\boldsymbol{F}}. \tag{2.50}$$

The *second Piola–Kirchhoff stress tensor* $\boldsymbol{S} : [0,\infty)\times\boldsymbol{\Phi}_t(\mathcal{B}_0) \to \mathbb{R}^{3\times3}$ is defined as

$$\boldsymbol{S}(t,\boldsymbol{X}) = \boldsymbol{F}^{-1}(t,\boldsymbol{X})\,\boldsymbol{P}(t,\boldsymbol{X}) = J(t,\boldsymbol{X})\,\boldsymbol{F}^{-1}(t,\boldsymbol{X})\,\boldsymbol{\sigma}(t,\boldsymbol{x})\,\boldsymbol{F}^{-\mathsf{T}}(t,\boldsymbol{X}), \tag{2.51}$$

leading to the important relation

$$\boldsymbol{P}(t,\boldsymbol{X}) = \boldsymbol{F}(t,\boldsymbol{X})\,\boldsymbol{S}(t,\boldsymbol{X}). \tag{2.52}$$

The second Piola–Kirchhoff stress tensor is also symmetric, therefore $\boldsymbol{S} = \boldsymbol{S}^{\mathsf{T}}$.

Newton's laws of motion can be generalized to a smooth deformable solid body with the balance laws for linear and angular momentum. From the balance of linear momentum, it follows that

$$\int_{\mathcal{B}_0} \varrho(t,\boldsymbol{X})\,\ddot{\boldsymbol{U}}(t,\boldsymbol{X})\,\mathrm{d}V = \int_{\partial\mathcal{B}_0} \bar{\boldsymbol{T}}(t,\boldsymbol{X})\,\mathrm{d}A + \int_{\mathcal{B}_0} \bar{\boldsymbol{B}}(t,\boldsymbol{X})\,\mathrm{d}V, \tag{2.53}$$

with the mass density $\varrho : [0,\infty)\times\mathcal{B}_0 \to \mathbb{R}$. With the relation of the first Piola–Kirchhoff stress tensor $\boldsymbol{P}$ and the traction force $\bar{\boldsymbol{T}}$ in Equation (2.47) and Gauss' divergence theorem, the internal forces can be written as

$$\int_{\partial\mathcal{B}_0} \bar{\boldsymbol{T}}(t,\boldsymbol{X})\,\mathrm{d}A = \int_{\mathcal{B}_0} \nabla\cdot\boldsymbol{P}(t,\boldsymbol{X})\,\mathrm{d}V. \tag{2.54}$$

Consequently, the balance of linear momentum in material form yields

$$\int_{\mathcal{B}_0} \rho(t,\boldsymbol{X})\ \ddot{\boldsymbol{U}}(t,\boldsymbol{X})\ \mathrm{d}V = \int_{\mathcal{B}_0} [\nabla \cdot \boldsymbol{P}(t,\boldsymbol{X}) + \overline{\boldsymbol{B}}(t,\boldsymbol{X})]\ \mathrm{d}V. \tag{2.55}$$

In the local form, it reads

$$\rho(t,\boldsymbol{X})\ \ddot{\boldsymbol{U}}(t,\boldsymbol{X}) = \ \nabla \cdot \boldsymbol{P}(t,\boldsymbol{X}) + \overline{\boldsymbol{B}}(t,\boldsymbol{X}) \qquad \forall (t,\boldsymbol{X}) \in [0,\infty) \times \mathcal{B}_0, \tag{2.56}$$

giving a relation between the acceleration and the internal and external forces acting on the body. It should be noted here that in Equation (2.56), Dirichlet and Neumann boundary conditions need to be considered for completeness.

3 | PERIDYNAMICS AS A NONLOCAL CONTINUUM THEORY

In this section, we aim to illustrate how different peridynamic formulations compute internal forces. This can be better understood by drawing an analogy between Cauchy's theorem in continuum mechanics and the peridynamic framework. While in Equation (2.45) the transmission of internal forces through a material body is described using the concept of stress tensors and traction forces, peridynamics generalizes this idea by considering nonlocal interactions over a finite horizon. This nonlocal averaging is performed in various ways, resulting in distinct peridynamics formulations.

3.1 | Nonlocal kinematics in peridynamics

In peridynamics, material points interact only with other points inside of their specified *neighborhood* or *point family* $\mathcal{H}$, which is defined as continuous set of infinite points inside a sphere with the radius $\delta \in \mathbb{R}^+$, also named the *horizon* δ, see Figure 5. The interaction of the point $\boldsymbol{X}$ with its neighbor $\boldsymbol{X}'$ is called *bond* $\boldsymbol{\Delta X} : \mathbb{R}^3 \times \mathbb{R}^3 \to \mathbb{R}^3$. In the reference configuration, a bond is defined as

$$\boldsymbol{\Delta X}(\boldsymbol{X},\boldsymbol{X}') = \boldsymbol{X}' - \boldsymbol{X}, \tag{3.1}$$

describing the vector that points from the point $\boldsymbol{X}$ to the point $\boldsymbol{X}'$. The related bond of the neighbor pointing from $\boldsymbol{X}'$ to $\boldsymbol{X}$ has the relation

$$\boldsymbol{\Delta X}(\boldsymbol{X}',\boldsymbol{X}) = -\boldsymbol{\Delta X}(\boldsymbol{X},\boldsymbol{X}') = \boldsymbol{X} - \boldsymbol{X}'. \tag{3.2}$$

In current configuration, the bond is defined as

$$\boldsymbol{\Delta x}(t,\boldsymbol{X},\boldsymbol{X}') = \boldsymbol{\Phi}(t,\boldsymbol{X}') - \boldsymbol{\Phi}(t,\boldsymbol{X}) = \boldsymbol{x}' - \boldsymbol{x}, \tag{3.3}$$

and also has the relation

$$\boldsymbol{\Delta x}(t,\boldsymbol{X}',\boldsymbol{X}) = -\boldsymbol{\Delta x}(t,\boldsymbol{X},\boldsymbol{X}') = \boldsymbol{x} - \boldsymbol{x}'. \tag{3.4}$$

For convenience, the notation $\boldsymbol{\Delta X} = \boldsymbol{\Delta X}(\boldsymbol{X},\boldsymbol{X}')$ and $\boldsymbol{\Delta x} = \boldsymbol{\Delta x}(t,\boldsymbol{X},\boldsymbol{X}')$ is also used in the following. The spherical neighborhood for the point $\boldsymbol{X}$ yields the continuous set

$$\mathcal{H}(\boldsymbol{X}) = \left\{\boldsymbol{X}' \in \mathcal{B}_0 \mid 0 < |\boldsymbol{\Delta X}| \leq \delta\right\}. \tag{3.5}$$

Analogously to Equation (3.1) and (3.3), the abbreviation $\boldsymbol{\Delta U}$ is introduced as

$$\boldsymbol{\Delta U} = \boldsymbol{\Delta U}(t,\boldsymbol{X},\boldsymbol{X}') = \boldsymbol{U}(t,\boldsymbol{X}') - \boldsymbol{U}(t,\boldsymbol{X}) \tag{3.6}$$

for notational simplification. The linear momentum balance in Equation (2.56) is in peridynamics defined as

$$\rho(t,\boldsymbol{X})\ \ddot{\boldsymbol{U}}(t,\boldsymbol{X}) = \overline{\boldsymbol{B}}^{\mathrm{int}}(t,\boldsymbol{X}) + \overline{\boldsymbol{B}}^{\mathrm{ext}}(t,\boldsymbol{X}) \qquad \forall (t,\boldsymbol{X}) \in [0,\infty) \times \mathcal{B}_0, \tag{3.7}$$

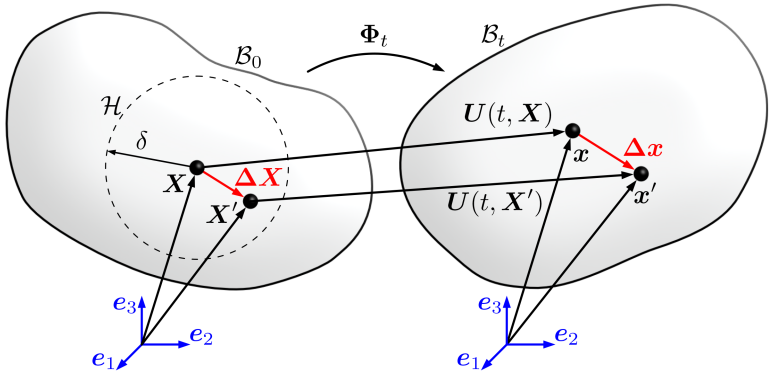

FIGURE 5 Deformation of a peridynamic body from the reference configuration $\mathcal{B}_0$ to the current configuration $\mathcal{B}_t$.

where $\overline{\boldsymbol{B}}^{\text{int}}(t,\boldsymbol{X}) = \nabla \cdot \boldsymbol{P}(t,\boldsymbol{X})$ corresponds to the divergence of the first Piola–Kirchhoff stress tensor. The term $\overline{\boldsymbol{B}}^{\text{int}}(t,\boldsymbol{X})$ is also called *internal body force density*. In statics, for homogeneous boundary values, the *external body force density* $\overline{\boldsymbol{B}}^{\text{ext}}(t,\boldsymbol{X}) = \overline{\boldsymbol{B}}(t,\boldsymbol{X})$ is equal to the material body forces in Equation (2.43).

3.2 | Simple linear elastic peridynamic constitutive models

The internal body force density $\overline{\boldsymbol{B}}^{\text{int}}$ can be approximated by a variety of peridynamic constitutive models, also called peridynamic formulations. The *bond-based formulation* is the simplest and most common model [33]. In the peridynamics community, this formulation is also called *prototype microelastic brittle* (PMB) model [32]. In bond-based peridynamics, each pair of material points interacts through a vector-valued function $\boldsymbol{f} : [0,\infty) \times \mathbb{R}^3 \times \mathbb{R}^3 \to \mathbb{R}^3$, such that the internal body force density $\overline{\boldsymbol{B}}^{\text{int}}(t,\boldsymbol{X})$ is approximated as

$$\overline{\boldsymbol{B}}^{\text{int}}(t,\boldsymbol{X}) = \int_{\mathcal{H}(\boldsymbol{X})} \boldsymbol{f}(t,\boldsymbol{X},\boldsymbol{X}')\, \mathrm{d}V' + \mathcal{O}(\delta^2). \tag{3.8}$$

The function $\boldsymbol{f}$ is also called *pairwise force function* and commonly defined as

$$\boldsymbol{f}(t,\boldsymbol{X},\boldsymbol{X}') = C_b\, \varepsilon_b(t,\boldsymbol{X},\boldsymbol{X}')\, \frac{\Delta\boldsymbol{x}}{|\Delta\boldsymbol{x}|}, \tag{3.9}$$

with the bond strain $\varepsilon_b : [0,\infty) \times \mathbb{R}^3 \times \mathbb{R}^3 \to \mathbb{R}$, calculated simply with

$$\varepsilon_b(t,\boldsymbol{X},\boldsymbol{X}') = \frac{|\Delta\boldsymbol{x}| - |\Delta\boldsymbol{X}|}{|\Delta\boldsymbol{X}|} = \frac{|\Delta\boldsymbol{x}|}{|\Delta\boldsymbol{X}|} - 1, \tag{3.10}$$

as the ratio of the bond elongation and the reference bond length. The bond constant C_b is defined as

$$C_b = \frac{18\,K}{\pi\,\delta^4}, \tag{3.11}$$

with the bulk modulus K.

An analogy can be established between the pairwise force function in Equation (3.9) and Cauchy's theorem in classical continuum mechanics in Equation (2.45), as both concepts describe the transmission of internal forces through a material body. The pairwise force function $\boldsymbol{f}$ could be considered a nonlocal analogue of the Cauchy stress tensor $\boldsymbol{\sigma}$. While $\bar{\boldsymbol{t}}$ represents a surface density of force, $\boldsymbol{f}$ expresses a volumetric density of interaction force distributed over the family $\mathcal{H}(\boldsymbol{X})$ within a finite horizon δ. In both Equation (2.54) and (3.8), the net internal force at a material point is obtained by combining directional contributions, either through the divergence of $\boldsymbol{P}$ in the classical theory or through the integral of $\boldsymbol{f}$ over $\mathcal{H}(\boldsymbol{X})$ in peridynamics. Although the formulations differ in being local and tensorial versus nonlocal and vector-valued, both approaches consistently describe the directional dependence and balance of internal forces in deformable continua.

The pairwise force function acts in the direction of the bond $\boldsymbol{\Delta x}$ and is proportional to the bond strain. With the definition of $\boldsymbol{f}$ in Equation (3.9), the condition

$$\boldsymbol{f}(t,\boldsymbol{X},\boldsymbol{X}') = -\boldsymbol{f}(t,\boldsymbol{X}',\boldsymbol{X}) \qquad \forall(\boldsymbol{X},\boldsymbol{X}') \in \mathcal{B}_0 \times \mathcal{H}(\boldsymbol{X}), \tag{3.12}$$

arises from Newton's third law of motion. Additionally, the conservation of angular momentum requires that the pairwise force function must be parallel to the current bond vector $\boldsymbol{\Delta x}$, leading to the condition

$$\boldsymbol{\Delta x} \times \boldsymbol{f}(t,\boldsymbol{X},\boldsymbol{X}') = \boldsymbol{0} \qquad \forall(\boldsymbol{X},\boldsymbol{X}') \in \mathcal{B}_0 \times \mathcal{H}(\boldsymbol{X}). \tag{3.13}$$

A significant limitation of bond-based peridynamics is that the elastic material behavior is governed by a single material parameter, as defined in Equation (3.11). Consequently, this imposes restrictions on Poisson's ratio, which follows as $\nu = 1/3$ in 2D and $\nu = 1/4$ in 3D [36]. To address this limitation, the state-based peridynamics theory was introduced [35], generalizing the formulation by allowing the internal force to depend on an averaged response from all bonds within the horizon. Consequently, the internal force density then depends on the averaged state of all neighboring points, leading to a more complex and flexible model. Here, the internal body force density $\overline{\boldsymbol{B}}^{\text{int}}$ is approximated as

$$\overline{\boldsymbol{B}}^{\text{int}}(t,\boldsymbol{X}) = \int_{\mathcal{H}(\boldsymbol{X})} \left(\boldsymbol{t}(t,\boldsymbol{X}',\boldsymbol{X}) - \boldsymbol{t}(t,\boldsymbol{X},\boldsymbol{X}')\right) \, \mathrm{d}V' + \mathcal{O}(\delta^2), \tag{3.14}$$

with the *force vector state* $\boldsymbol{t} : [0,\infty) \times \mathbb{R}^3 \times \mathbb{R}^3 \to \mathbb{R}^3$.

There are various approaches and constitutive models to define the force vector state $\boldsymbol{t}$. The most common model is the *linear peridynamic solid* (LPS) model, also referred to as *ordinary state-based* (OSB) peridynamics [35]. Specifically, it introduces a decomposition of the force into volumetric (isotropic) and shear (deviatoric) contributions, each controlled by the material parameters bulk modulus K and shear modulus G. This enables the representation of a full range of elastic constants, making the model consistent with classical linear elasticity in the limit of a vanishing horizon $\delta \to 0$.

The LPS is an *ordinary* model because the force vector state $\boldsymbol{t}$ is parallel to the current bond vector $\boldsymbol{\Delta x}$ and can be expressed as

$$\boldsymbol{t}(t,\boldsymbol{X},\boldsymbol{X}') = \tilde{t}(t,\boldsymbol{X},\boldsymbol{X}') \, \frac{\boldsymbol{\Delta x}}{|\boldsymbol{\Delta x}|}, \tag{3.15}$$

where $\tilde{t} : [0,\infty) \times \mathbb{R}^3 \times \mathbb{R}^3 \to \mathbb{R}$ is a scalar-valued force state function. As mentioned before, the scalar-valued force state function can be expressed as a combination of the deviatoric and isotropic components

$$\tilde{t}(t,\boldsymbol{X},\boldsymbol{X}') = \tilde{t}_{\text{iso}}(t,\boldsymbol{X},\boldsymbol{X}') + \tilde{t}_{\text{dev}}(t,\boldsymbol{X},\boldsymbol{X}'). \tag{3.16}$$

To calculate these components, the LPS model uses the dilatation $\theta(t,\boldsymbol{X})$, which is a measure of volumetric deformation. The weighted volume m is used to normalize the dilatation and is defined as the constant

$$m(\boldsymbol{X}) = \int_{\mathcal{H}(\boldsymbol{X})} \omega(\boldsymbol{\Delta X})|\boldsymbol{\Delta X}|^2 \, \mathrm{d}V', \tag{3.17}$$

averaged over the point family $\mathcal{H}(\boldsymbol{X})$. Averaging over the point family is done using a kernel function $\omega : \left\{\mathbb{R}^3 \setminus \boldsymbol{0}\right\} \to [0,\infty)$ with $\omega(\boldsymbol{\Delta X}) = 0$ for $|\boldsymbol{\Delta X}| > \delta$. In the peridynamics community, ω is often called *influence function* and chosen as a positive, radial function decaying with distance. With these quantities, the dilatation $\theta(t,\boldsymbol{X})$ is defined as

$$\theta(t,\boldsymbol{X}) = \frac{3}{m(\boldsymbol{X})} \int_{\mathcal{H}(\boldsymbol{X})} \omega(\boldsymbol{\Delta X})(|\boldsymbol{\Delta x}| - |\boldsymbol{\Delta X}|)|\boldsymbol{\Delta X}| \, \mathrm{d}V'. \tag{3.18}$$

With the weighted volume and the dilatation, the isotropic part of the scalar force density is defined as

$$\tilde{t}_{\text{iso}}(t,\boldsymbol{X},\boldsymbol{X}') = \omega(\boldsymbol{\Delta X}) \frac{3\,K}{m(\boldsymbol{X})} \, \theta(t,\boldsymbol{X}) \, |\boldsymbol{\Delta X}|, \tag{3.19}$$

and the remaining deviatoric part as

$$\tilde{t}_{\text{dev}}(t,\boldsymbol{X},\boldsymbol{X}') = \omega(\boldsymbol{\Delta X})\frac{15\ G}{m(\boldsymbol{X})}\Big(|\boldsymbol{\Delta x}| - |\boldsymbol{\Delta X}| - \frac{1}{3}\theta(t,\boldsymbol{X})|\boldsymbol{\Delta X}|\Big). \tag{3.20}$$

The LPS model not only overcomes the limitations of bond-based peridynamics but also ensures frame invariance, objectivity, and angular momentum conservation through its symmetric force construction and alignment of internal forces with bond directions. This makes the LPS model a straightforward yet powerful extension of the bond-based formulation, capable of modeling general isotropic elastic solids while maintaining consistency with classical linear elasticity.

The introduced PMB model is a special case of the LPS model, as shown by [30]. A Poisson's ratio of $\nu = 1/4$ in a three-dimensional setting leads to the relation

$$G = \frac{3}{5}K. \tag{3.21}$$

With this relation, the scalar force state in Equation (3.15) can be rewritten as

$$\begin{aligned}
\tilde{t}(t,\boldsymbol{X},\boldsymbol{X}') &= \omega(\boldsymbol{\Delta X})\frac{3\ K}{m(\boldsymbol{X})}\ \theta(t,\boldsymbol{X})\ |\boldsymbol{\Delta X}| + \omega(\boldsymbol{\Delta X})\frac{9\ K}{m(\boldsymbol{X})}\Big(|\boldsymbol{\Delta x}| - |\boldsymbol{\Delta X}| - \frac{1}{3}\theta(t,\boldsymbol{X})|\boldsymbol{\Delta X}|\Big)\\
&= \omega(\boldsymbol{\Delta X})\frac{K}{m(\boldsymbol{X})}\Big[3\ \theta(t,\boldsymbol{X})\ |\boldsymbol{\Delta X}| + 9\Big(|\boldsymbol{\Delta x}| - |\boldsymbol{\Delta X}| - \frac{1}{3}\theta(t,\boldsymbol{X})|\boldsymbol{\Delta X}|\Big)\Big]\\
&= \omega(\boldsymbol{\Delta X})\frac{K}{m(\boldsymbol{X})}(3\ \theta(t,\boldsymbol{X})\ |\boldsymbol{\Delta X}| + 9(|\boldsymbol{\Delta x}| - |\boldsymbol{\Delta X}|) - 3\ \theta(t,\boldsymbol{X})|\boldsymbol{\Delta X}|)\\
&= \omega(\boldsymbol{\Delta X})\frac{9\ K}{m(\boldsymbol{X})}(|\boldsymbol{\Delta x}| - |\boldsymbol{\Delta X}|).
\end{aligned}$$

When choosing the kernel to be the spherical function $\omega(\boldsymbol{\Delta X}) = 1/|\boldsymbol{\Delta X}|$ in $\mathcal{H}(\boldsymbol{X})$, the weighted volume yields for $\mathcal{H} \subset \mathcal{B}_0$

$$m(\boldsymbol{X}) = \int_{\mathcal{H}(\boldsymbol{X})} \frac{1}{|\boldsymbol{\Delta X}|}|\boldsymbol{\Delta X}|^2\ \mathrm{d}V' = \int_{\mathcal{H}(\boldsymbol{X})} |\boldsymbol{\Delta X}|\ \mathrm{d}V' = \pi\delta^4, \tag{3.22}$$

where the integral is performed over a spherical neighborhood of radius δ. With the specific kernel function and the simplified weighted volume, the scalar force state becomes

$$\tilde{t}(t,\boldsymbol{X},\boldsymbol{X}') = \frac{9\ K}{\pi\delta^4}\left(\frac{|\boldsymbol{\Delta x}| - |\boldsymbol{\Delta X}|}{|\boldsymbol{\Delta X}|}\right) = \frac{9\ K}{\pi\delta^4}\varepsilon_b(t,\boldsymbol{X},\boldsymbol{X}'),$$

recovering the PMB model by giving the relation

$$\boldsymbol{t}(t,\boldsymbol{X},\boldsymbol{X}') = \frac{1}{2}\boldsymbol{f}(t,\boldsymbol{X},\boldsymbol{X}'), \tag{3.23}$$

where the factor of $1/2$ arises from the definition of the pairwise force function in Equation (3.9).

Both the LPS and PMB models are inherently linear elastic formulations. A more rigorous approach in accordance with classical continuum mechanics is achieved by the *correspondence formulation* (CC) [35].

In the correspondence formulation, the constitutive response at each material point is evaluated through a classical local model, such as the Saint Venant–Kirchhoff model used in this work. The notions of variational consistency and polyconvexity therefore apply at the level of the local strain-energy density, and the formulation inherits the analytical properties of the chosen local model.

3.3 | Approximation of the deformation gradient

The correspondence formulation in peridynamics approximates the deformation gradient and stress measures using nonlocal interactions. This approach enables the incorporation of constitutive models from classical mechanics into the peridynamic framework.

In the correspondence formulation, an approximated deformation gradient $\overline{\boldsymbol{F}}$ is defined with an approximated displacement gradient $\overline{\nabla}\boldsymbol{U}$ as

$$\overline{\boldsymbol{F}}(t,\boldsymbol{X}) = \boldsymbol{I} + \overline{\nabla}\boldsymbol{U}(t,\boldsymbol{X}), \tag{3.24}$$

recovering Equation (2.17) with

$$\boldsymbol{F}(t,\boldsymbol{X}) = \overline{\boldsymbol{F}}(t,\boldsymbol{X}) + \mathcal{O}(\delta^2), \qquad \nabla\boldsymbol{U}(t,\boldsymbol{X}) = \overline{\nabla}\boldsymbol{U}(t,\boldsymbol{X}) + \mathcal{O}(\delta^2). \tag{3.25}$$

To derive $\overline{\boldsymbol{F}}$, the displacement of the neighbor point can be approximated with a Taylor approximation by neglecting higher order terms as

$$\boldsymbol{U}(t,\boldsymbol{X}') = \boldsymbol{U}(t,\boldsymbol{X}) + \overline{\nabla}\boldsymbol{U}(t,\boldsymbol{X})\Delta\boldsymbol{X}, \tag{3.26}$$

with the transformation

$$\overline{\nabla}\boldsymbol{U}(t,\boldsymbol{X})\left(\boldsymbol{X}' - \boldsymbol{X}\right) = \boldsymbol{U}(t,\boldsymbol{X}') - \boldsymbol{U}(t,\boldsymbol{X}), \tag{3.27}$$

or shortly,

$$\overline{\nabla}\boldsymbol{U}\Delta\boldsymbol{X} = \Delta\boldsymbol{U}. \tag{3.28}$$

A tensor product of Equation (3.27) with $\Delta\boldsymbol{X}$ in the limit of $\boldsymbol{X}' \to \boldsymbol{X}$ yields

$$\lim_{\boldsymbol{X}'\to\boldsymbol{X}} \left(\overline{\nabla}\boldsymbol{U}\Delta\boldsymbol{X} \otimes \Delta\boldsymbol{X} - \Delta\boldsymbol{U} \otimes \Delta\boldsymbol{X}\right) = \boldsymbol{0}. \tag{3.29}$$

Averaging $\overline{\nabla}\boldsymbol{U}\Delta\boldsymbol{X} \otimes \Delta\boldsymbol{X}$ over the family $\mathcal{H}$ gives

$$\int_{\mathcal{H}(\boldsymbol{X})} \omega(\Delta\boldsymbol{X})\, \overline{\nabla}\boldsymbol{U}(t,\boldsymbol{X})\, \Delta\boldsymbol{X} \otimes \Delta\boldsymbol{X}\, \mathrm{d}V' = \int_{\mathcal{H}(\boldsymbol{X})} \omega(\Delta\boldsymbol{X})\, \Delta\boldsymbol{U} \otimes \Delta\boldsymbol{X}\, \mathrm{d}V'. \tag{3.30}$$

Rearranging, a shape tensor $\boldsymbol{K}$ can be defined as

$$\boldsymbol{K}(\boldsymbol{X}) = \int_{\mathcal{H}(\boldsymbol{X})} \omega(\Delta\boldsymbol{X})\, \Delta\boldsymbol{X} \otimes \Delta\boldsymbol{X}\, \mathrm{d}V'. \tag{3.31}$$

It can be observed that $\boldsymbol{K}$ is a symmetric and positive definite matrix in $\mathbb{R}^{3\times3}$. This leads to the simplification of Equation (3.30) as

$$\overline{\nabla}\boldsymbol{U}(t,\boldsymbol{X})\boldsymbol{K}(\boldsymbol{X}) = \int_{\mathcal{H}(\boldsymbol{X})} \omega(\Delta\boldsymbol{X})\, \Delta\boldsymbol{U} \otimes \Delta\boldsymbol{X}\, \mathrm{d}V', \tag{3.32}$$

and to the definition of the approximated displacement gradient

$$\overline{\nabla}\boldsymbol{U}(t,\boldsymbol{X}) = \left(\int_{\mathcal{H}(\boldsymbol{X})} \omega(\Delta\boldsymbol{X})\, \Delta\boldsymbol{U} \otimes \Delta\boldsymbol{X}\, \mathrm{d}V' \right) \boldsymbol{K}^{-1}(\boldsymbol{X}). \tag{3.33}$$

With Equation (3.24) and (3.33), the approximated deformation gradient can be written as

$$\begin{aligned} \overline{\boldsymbol{F}}(t,\boldsymbol{X}) &= \left(\boldsymbol{K}(\boldsymbol{X}) + \int_{\mathcal{H}(\boldsymbol{X})} \omega(\Delta\boldsymbol{X})\, \Delta\boldsymbol{U} \otimes \Delta\boldsymbol{X}\, \mathrm{d}V' \right) \boldsymbol{K}^{-1}(\boldsymbol{X}) \\ &= \left(\int_{\mathcal{H}(\boldsymbol{X})} \omega(\Delta\boldsymbol{X})\, \Delta\boldsymbol{x} \otimes \Delta\boldsymbol{X}\, \mathrm{d}V' \right) \boldsymbol{K}^{-1}(\boldsymbol{X}), \end{aligned} \tag{3.34}$$

with the relation $\Delta\boldsymbol{X} + \Delta\boldsymbol{U} = \boldsymbol{\Phi}(t,\boldsymbol{X}') - \boldsymbol{\Phi}(t,\boldsymbol{X}) = \Delta\boldsymbol{x}$. The deformation gradient therefore is finally approximated as

$$\boldsymbol{F}(t,\boldsymbol{X}) = \left(\int_{\mathcal{H}(\boldsymbol{X})} \omega(\Delta\boldsymbol{X})\, \Delta\boldsymbol{x} \otimes \Delta\boldsymbol{X}\, \mathrm{d}V' \right) \boldsymbol{K}^{-1}(\boldsymbol{X}) + \mathcal{O}(\delta^2). \tag{3.35}$$

3.4 | Approximation of the stress forces

With the help of the deformation gradient $\overline{\boldsymbol{F}}$, the stress forces can be approximated. We assume that the reference domain $\mathcal{B}_0$ is a bounded Lipschitz domain with boundary $\partial\mathcal{B}_0$. To derive the stress forces, multiplication of Equation (2.56) with a test function $\boldsymbol{w}$ and integration over the body $\mathcal{B}_0$ by parts yields the variational form

$$\int_{\mathcal{B}_0} \varrho(t,\boldsymbol{X})\, \ddot{\boldsymbol{U}}(t,\boldsymbol{X}) \cdot \boldsymbol{w}(\boldsymbol{X})\, \mathrm{d}V = \int_{\mathcal{B}_0} \boldsymbol{P}(t,\boldsymbol{X}) : \nabla \boldsymbol{w}(\boldsymbol{X})\, \mathrm{d}V + \int_{\mathcal{B}_0} \overline{\boldsymbol{B}}^{\mathrm{ext}}(t,\boldsymbol{X}) \cdot \boldsymbol{w}(\boldsymbol{X})\, \mathrm{d}V \tag{3.36}$$

for all $t \in (0,T)$, smooth test functions $\boldsymbol{w} : \overline{\mathcal{B}_0} \to \mathbb{R}^3$ with $\boldsymbol{w}(\boldsymbol{X}) = \boldsymbol{0}$ for $\boldsymbol{X} \in \partial\mathcal{B}_0$, and the first Piola–Kirchhoff stress tensor $\boldsymbol{P}(t,\boldsymbol{X}) = \boldsymbol{P}(\boldsymbol{F}(t,\boldsymbol{X}))$.

The Taylor approximation of the test function at $\boldsymbol{X}$ yields

$$\boldsymbol{w}(\boldsymbol{X}') = \boldsymbol{w}(\boldsymbol{X}) + \nabla \boldsymbol{w}(\boldsymbol{X})\Delta\boldsymbol{X} + \mathcal{O}(|\Delta\boldsymbol{X}|^2) \tag{3.37}$$

with the transformation

$$\nabla \boldsymbol{w}(\boldsymbol{X})\Delta\boldsymbol{X} = \boldsymbol{w}(\boldsymbol{X}') - \boldsymbol{w}(\boldsymbol{X}) + \mathcal{O}(|\Delta\boldsymbol{X}|^2) = \Delta\boldsymbol{w} + \mathcal{O}(|\Delta\boldsymbol{X}|^2),$$

and $\Delta\boldsymbol{w} = \boldsymbol{w}(\boldsymbol{X}') - \boldsymbol{w}(\boldsymbol{X})$. Multiplication of the gradient $\nabla\boldsymbol{w}$ with the shape tensor

$$\nabla \boldsymbol{w}(\boldsymbol{X})\boldsymbol{K}(\boldsymbol{X}) = \int_{\mathcal{H}(\boldsymbol{X})} \omega(\Delta\boldsymbol{X})\, \Delta\boldsymbol{w} \otimes \Delta\boldsymbol{X}\, \mathrm{d}V' + \mathcal{O}(\delta^2)$$

gives

$$\nabla \boldsymbol{w}(\boldsymbol{X}) = \left(\int_{\mathcal{H}(\boldsymbol{X})} \omega(\Delta\boldsymbol{X})\, \Delta\boldsymbol{w} \otimes \Delta\boldsymbol{X}\, \mathrm{d}V' \right) \boldsymbol{K}^{-1}(\boldsymbol{X}) + \mathcal{O}(\delta^2). \tag{3.38}$$

Since the shape tensor $\boldsymbol{K}(\boldsymbol{X})$ is symmetric, it follows

$$\begin{aligned}
\int_{\mathcal{B}_0} \boldsymbol{P}(t,\boldsymbol{X}) : \nabla \boldsymbol{w}(\boldsymbol{X})\, \mathrm{d}V &= \int_{\mathcal{B}_0} \boldsymbol{P}(t,\boldsymbol{X}) : \left(\int_{\mathcal{H}(\boldsymbol{X})} \omega(\Delta\boldsymbol{X})\, \Delta\boldsymbol{w} \otimes \Delta\boldsymbol{X}\, \boldsymbol{K}^{-1}(\boldsymbol{X})\, \mathrm{d}V' \right) \mathrm{d}V + \mathcal{O}(\delta^2) \\
&= \int_{\mathcal{B}_0} \int_{\mathcal{H}(\boldsymbol{X})} \omega(\Delta\boldsymbol{X})\, \boldsymbol{P}(t,\boldsymbol{X}) : \left(\Delta\boldsymbol{w} \otimes \Delta\boldsymbol{X}\, \boldsymbol{K}^{-1}(\boldsymbol{X}) \right) \mathrm{d}V'\, \mathrm{d}V + \mathcal{O}(\delta^2) \\
&= \int_{\mathcal{B}_0} \int_{\mathcal{H}(\boldsymbol{X})} \omega(\Delta\boldsymbol{X}) \left(\boldsymbol{P}(t,\boldsymbol{X})\, \boldsymbol{K}^{-1}(\boldsymbol{X}) \right) : (\Delta\boldsymbol{w} \otimes \Delta\boldsymbol{X})\, \mathrm{d}V'\, \mathrm{d}V + \mathcal{O}(\delta^2) \\
&= \int_{\mathcal{B}_0} \int_{\mathcal{H}(\boldsymbol{X})} \left(\omega(\Delta\boldsymbol{X}) \boldsymbol{P}(t,\boldsymbol{X})\, \boldsymbol{K}^{-1}(\boldsymbol{X}) \Delta\boldsymbol{X} \right) \cdot \Delta\boldsymbol{w}\, \mathrm{d}V'\, \mathrm{d}V + \mathcal{O}(\delta^2).
\end{aligned}$$

The traction forces, which are also called the *force vector state* $\boldsymbol{t}$, can be defined as

$$\boldsymbol{t}(t,\boldsymbol{X},\boldsymbol{X}') = \omega(\Delta\boldsymbol{X})\, \boldsymbol{P}(t,\boldsymbol{X})\, \boldsymbol{K}^{-1}(\boldsymbol{X}) \Delta\boldsymbol{X}(\boldsymbol{X},\boldsymbol{X}'), \tag{3.39}$$

which, with $\Delta\boldsymbol{w} = \boldsymbol{w}(\boldsymbol{X}') - \boldsymbol{w}(\boldsymbol{X})$, leads to

$$\begin{aligned}
\int_{\mathcal{B}_0} \boldsymbol{P}(t,\boldsymbol{X}) : \nabla \boldsymbol{w}(\boldsymbol{X})\, \mathrm{d}V &= \int_{\mathcal{B}_0} \int_{\mathcal{H}(\boldsymbol{X})} \boldsymbol{t}(t,\boldsymbol{X},\boldsymbol{X}') \cdot \left(\boldsymbol{w}(\boldsymbol{X}') - \boldsymbol{w}(\boldsymbol{X}) \right) \mathrm{d}V'\, \mathrm{d}V + \mathcal{O}(\delta^2) \\
&= \int_{\mathcal{B}_0} \int_{\mathcal{H}(\boldsymbol{X})} \boldsymbol{t}(t,\boldsymbol{X},\boldsymbol{X}') \cdot \boldsymbol{w}(\boldsymbol{X}')\, \mathrm{d}V'\, \mathrm{d}V - \int_{\mathcal{B}_0} \int_{\mathcal{H}(\boldsymbol{X})} \boldsymbol{t}(t,\boldsymbol{X},\boldsymbol{X}') \cdot \boldsymbol{w}(\boldsymbol{X})\, \mathrm{d}V'\, \mathrm{d}V + \mathcal{O}(\delta^2) \\
&= \int_{\mathcal{B}_0} \int_{\mathcal{H}(\boldsymbol{X})} \boldsymbol{t}(t,\boldsymbol{X}',\boldsymbol{X}) \cdot \boldsymbol{w}(\boldsymbol{X})\, \mathrm{d}V\, \mathrm{d}V' - \int_{\mathcal{B}_0} \int_{\mathcal{H}(\boldsymbol{X})} \boldsymbol{t}(t,\boldsymbol{X},\boldsymbol{X}') \cdot \boldsymbol{w}(\boldsymbol{X})\, \mathrm{d}V'\, \mathrm{d}V + \mathcal{O}(\delta^2) \\
&= \int_{\mathcal{B}_0} \left(\int_{\mathcal{H}(\boldsymbol{X})} \left(\boldsymbol{t}(t,\boldsymbol{X}',\boldsymbol{X}) - \boldsymbol{t}(t,\boldsymbol{X},\boldsymbol{X}') \right) \mathrm{d}V' \right) \cdot \boldsymbol{w}(\boldsymbol{X})\, \mathrm{d}V + \mathcal{O}(\delta^2),
\end{aligned}$$

and together

$$\int_{\mathcal{B}_0} \left(\rho(t,\boldsymbol{X})\ \ddot{\boldsymbol{U}}(t,\boldsymbol{X}) - \int_{\mathcal{H}(\boldsymbol{X})} \left(\boldsymbol{t}(t,\boldsymbol{X}',\boldsymbol{X}) - \boldsymbol{t}(t,\boldsymbol{X},\boldsymbol{X}') \right) \mathrm{d}V' - \overline{\boldsymbol{B}}^{\mathrm{ext}}(t,\boldsymbol{X}) \right) \cdot \boldsymbol{w}(\boldsymbol{X})\ \mathrm{d}V = \mathcal{O}(\delta^2). \tag{3.40}$$

This holds for all smooth test functions with homogeneous boundary values, so that we finally get for interior points

$$\rho(t,\boldsymbol{X})\ \ddot{\boldsymbol{U}}(t,\boldsymbol{X}) = \int_{\mathcal{H}(\boldsymbol{X})} \left(\boldsymbol{t}(t,\boldsymbol{X}',\boldsymbol{X}) - \boldsymbol{t}(t,\boldsymbol{X},\boldsymbol{X}') \right) \mathrm{d}V' + \overline{\boldsymbol{B}}^{\mathrm{ext}}(t,\boldsymbol{X}) + \mathcal{O}(\delta^2) \qquad \forall \boldsymbol{X} \in \mathcal{B}_0. \tag{3.41}$$

Therefore, the divergence of the first Piola–Kirchhoff stress tensor can be approximated as

$$\nabla \cdot \boldsymbol{P}(t,\boldsymbol{X}) = \int_{\mathcal{H}(\boldsymbol{X})} \left(\boldsymbol{t}(t,\boldsymbol{X}',\boldsymbol{X}) - \boldsymbol{t}(t,\boldsymbol{X},\boldsymbol{X}') \right) \mathrm{d}V' + \mathcal{O}(\delta^2), \tag{3.42}$$

recovering Equation (3.14). The comparison with Equation (3.42) shows that the correspondence formulation is equivalent to the LPS model in one aspect, as it approximates the internal force density of a point considering the state of all its neighbors.

3.5 | Reproducing kernel approximation

The previously derived equations of the correspondence formulation are based on a Taylor approximation of the displacement gradient and the stress forces. However, it can be shown that the approximation of the displacement gradient and the stress forces can be derived from a reproducing kernel (RK) approximation [17]. The RK approximation is a powerful method for approximating functions and their derivatives using a set of basis functions, known as reproducing kernels. It has its roots in the reproducing kernel particle method (RKPM) [24], which is a meshless method for solving partial differential equations.

The correspondence formulation can be written in terms of a RK approximation. The RK peridynamics formulation is based on a nonlocal gradient operator utilizing $[n]^{\mathrm{th}}$-order accuracy in approximating local gradients [2, 17]. When utilizing reproducing kernels, Equation (3.33) can be written as

$$\overline{\nabla} \boldsymbol{U}(t,\boldsymbol{X}) = \int_{\mathcal{H}(\boldsymbol{X})} \Delta \boldsymbol{U} \otimes \boldsymbol{\Psi}_{[n]}(\boldsymbol{X},\boldsymbol{X}')\ \mathrm{d}V', \tag{3.43}$$

with the RK gradient operator $\boldsymbol{\Psi}_{[n]}$. This operator is defined as

$$\boldsymbol{\Psi}_{[n]}(\boldsymbol{X},\boldsymbol{X}') = \omega(\Delta\boldsymbol{X})\ \boldsymbol{Q}^{\nabla}_{[n]}\ \boldsymbol{M}^{-1}_{[n]}(\boldsymbol{X})\ \boldsymbol{Q}_{[n]}(\Delta\boldsymbol{X}), \tag{3.44}$$

with the monomial vector $\boldsymbol{Q}_{[n]} : \mathbb{R}^3 \to \mathbb{R}^m$, which contains m monomials of a given order n in the spatial coordinates, and the moment matrix $\boldsymbol{M}_{[n]} : \mathbb{R}^3 \to \mathbb{R}^{m \times m}$, which is defined as

$$\boldsymbol{M}_{[n]}(\boldsymbol{X}) = \int_{\mathcal{H}(\boldsymbol{X})} \omega(\Delta\boldsymbol{X})\ \boldsymbol{Q}_{[n]}(\Delta\boldsymbol{X}) \otimes \boldsymbol{Q}_{[n]}(\Delta\boldsymbol{X})\ \mathrm{d}V'. \tag{3.45}$$

In three-dimensional space, for instance, $\boldsymbol{Q}_{[n]}$ includes linear and quadratic terms depending on the value of n. The term $\boldsymbol{Q}^{\nabla}_{[n]}$ plays a critical role in selecting the target derivative in the RK approximation. It encodes the direction and order of the derivative being reproduced. This matrix, often sparse, consists of zero entries except for a unit coefficient (or factorial weight) at the position corresponding to the desired monomial basis function. Specifically, each row of $\boldsymbol{Q}^{\nabla}_{[n]}$ corresponds to a Cartesian derivative direction [17]. In three-dimensional space, the target derivative matrix $\boldsymbol{Q}^{\nabla}_{[n]}$ takes the form

$$\boldsymbol{Q}^{\nabla}_{[n]} = \left[\frac{\partial \boldsymbol{Q}_{[n]}(\boldsymbol{0})}{\partial X_1} \quad \frac{\partial \boldsymbol{Q}_{[n]}(\boldsymbol{0})}{\partial X_2} \quad \frac{\partial \boldsymbol{Q}_{[n]}(\boldsymbol{0})}{\partial X_3} \right]^{\mathsf{T}}. \tag{3.46}$$

For the linear case ($n = 1$), a monomial vector in three-dimensional space can be given as

$$\boldsymbol{Q}_{[1]}(\boldsymbol{X}) = \begin{bmatrix} X_1 & X_2 & X_3 \end{bmatrix}^{\mathsf{T}}, \tag{3.47}$$

with $\boldsymbol{Q}_{[1]}(\boldsymbol{\Delta X}) = \boldsymbol{\Delta X}$, which yields $\boldsymbol{M}_{[1]}(\boldsymbol{X}) = \boldsymbol{K}(\boldsymbol{X})$, and

$$\boldsymbol{Q}^{\nabla}_{[1]} = \begin{bmatrix} 1 & 0 & 0 \\ 0 & 1 & 0 \\ 0 & 0 & 1 \end{bmatrix} = \boldsymbol{I}. \tag{3.48}$$

Therefore, the RK gradient operator with first-order accuracy simplifies to

$$\boldsymbol{\Psi}_{[1]}(\boldsymbol{X}, \boldsymbol{X}') = \omega(\boldsymbol{\Delta X})\, \boldsymbol{K}^{-1}(\boldsymbol{X})\, \boldsymbol{\Delta X}, \tag{3.49}$$

restoring Equation (3.43) as Equation (3.33), since the shape tensor $\boldsymbol{K}$ is symmetric. For readability, the index $[n]$ is omitted in the following. With this definition of the RK gradient operator, Equation (3.34) can be rewritten as

$$\overline{\boldsymbol{F}}(t, \boldsymbol{X}) = \int_{\mathcal{H}(\boldsymbol{X})} \boldsymbol{\Delta x} \otimes \boldsymbol{\Psi}(\boldsymbol{X}, \boldsymbol{X}')\, \mathrm{d}V'. \tag{3.50}$$

Also the approximation of the stress forces can be written in terms of the gradient operator, rewriting Equation (3.42) as

$$\nabla \cdot \boldsymbol{P}(t, \boldsymbol{X}) = \int_{\mathcal{H}(\boldsymbol{X})} \big(\boldsymbol{P}(t, \boldsymbol{X}') - \boldsymbol{P}(t, \boldsymbol{X})\big)\boldsymbol{\Psi}(\boldsymbol{X}, \boldsymbol{X}')\, \mathrm{d}V' + \mathcal{O}(\delta^2). \tag{3.51}$$

Consequently, it can be shown that the standard correspondence model can be reformulated in terms of a RK approximation, similar to the RKPM.

For monomials of second order ($n = 2$), a monomial vector in three-dimensional space can be defined as

$$\boldsymbol{Q}_{[2]}(\boldsymbol{X}) = \begin{bmatrix} X_1 & X_2 & X_3 & X_1^2 & X_2^2 & X_3^2 & X_1X_2 & X_1X_3 & X_2X_3 \end{bmatrix}^{\mathsf{T}}, \tag{3.52}$$

with the corresponding target derivative matrix

$$\boldsymbol{Q}^{\nabla}_{[2]} = \begin{bmatrix} 1 & 0 & 0 & 0 & 0 & 0 & 0 & 0 & 0 \\ 0 & 1 & 0 & 0 & 0 & 0 & 0 & 0 & 0 \\ 0 & 0 & 1 & 0 & 0 & 0 & 0 & 0 & 0 \end{bmatrix}. \tag{3.53}$$

It can be shown that the RK approach with second-order accuracy leads to a more precise approximation of the deformation gradient [2, 17].

3.6 | Spatial discretization

The continuous peridynamic formulation requires discretization for numerical implementation. Unlike classical finite element methods that rely on mesh connectivity, peridynamics naturally lends itself to particle-based discretization schemes where material points interact through nonlocal bonds within their horizons. This meshfree character simplifies the treatment of discontinuities and crack propagation, as no special remeshing or enrichment techniques are required when material failure occurs.

A discretized peridynamic body $\mathcal{B}_0^N = \{\boldsymbol{X}_k \in \mathcal{B}_0 \mid k = 1, \ \dots \ , N\}$ is defined as a set of N finite points in the reference domain $\mathcal{B}_0$. The spatial arrangement of these points is typically characterized by a uniform point spacing $\vartriangle x$, representing the distance between neighboring points in the initial configuration. In the discrete form, a point $\boldsymbol{X}_k$ and its neighbor $\boldsymbol{X}_n$

form the bond

$$\Delta \boldsymbol{X}_{kn} = \boldsymbol{X}_n - \boldsymbol{X}_k, \tag{3.54}$$

which yields the neighborhood

$$\mathcal{H}^N = \mathcal{H}^N(\boldsymbol{X}_k) = \left\{ \boldsymbol{X}_n \in \mathcal{B}_0^N \mid 0 \leq |\Delta \boldsymbol{X}_{kn}| \leq \delta \right\}. \tag{3.55}$$

For discrete functions $\phi : \mathcal{H}^N \to \mathbb{R}$, the integral over the neighborhood can be approximated by a weighted sum over all neighbors as

$$\int_{\mathcal{H}(\boldsymbol{X})} \omega(\Delta \boldsymbol{X})\ \phi(\boldsymbol{X}')\ \mathrm{d}V' = \sum_{\boldsymbol{X}_n \in \mathcal{H}^N} \omega(\Delta \boldsymbol{X})\ \phi(\boldsymbol{X}_n)\ V_n, \tag{3.56}$$

with the volume $V : \mathcal{B}_0^N \to \mathbb{R}^+$ and $V_n = V(\boldsymbol{X}_n)$ and the condition

$$V(\mathcal{B}^N) = \sum_{\boldsymbol{X}_n \in \mathcal{B}_0^N} V_n. \tag{3.57}$$

3.7 | Temporal discretization with Velocity-Verlet

The time evolution of peridynamic systems requires appropriate temporal discretization schemes to ensure numerical stability and accuracy. Explicit time integration methods are commonly employed in peridynamics due to their computational efficiency and straightforward implementation, particularly when dealing with dynamic fracture problems where wave propagation phenomena dominate the response. If the simulation time T is small, then explicit time integration is a viable option. In peridynamics, the Velocity-Verlet algorithm [15, 23, 26, 38] is the most widely used explicit time integration schemes. The time step $\triangle t$ is defined as $\triangle t = \frac{T}{N_T}$, with the number of time steps N_T. The time at a specific time step n is defined as $t_n = n\ \triangle t$. The time step $\triangle t$ is in peridynamics often calculated with a stability approach. In this approach, the critical time step for a point k is calculated as

$$\triangle t_k(\boldsymbol{X}_k) = \sqrt{\frac{2\ \rho_0}{\sum_{\boldsymbol{X}_n \in \mathcal{H}^N} \frac{C_b\ V_n}{|\Delta \boldsymbol{X}_{kn}|}}}, \tag{3.58}$$

with the density ρ_0 and the bond-constant $C_b = \frac{18\ K}{\pi\ \delta^4}$ with bulk modulus K. Then the critical time step $\triangle t$ for the simulation is defined as the minimum of all $\triangle t_k$

$$\triangle t = \min_{\boldsymbol{X}_k \in \mathcal{B}^N} \triangle t_k(\boldsymbol{X}_k). \tag{3.59}$$

In the Velocity-Verlet algorithm, the acceleration $\ddot{\boldsymbol{U}}$, velocity $\dot{\boldsymbol{U}}$ and displacement $\boldsymbol{U}$ are forward calculated with the following scheme.

(S0) Set the initial values for displacement $\boldsymbol{U}_0$, velocity $\dot{\boldsymbol{U}}_0$, and acceleration $\ddot{\boldsymbol{U}}_0$ as

$$\boldsymbol{U}(0, \boldsymbol{X}) = \boldsymbol{U}_0(\boldsymbol{X}), \quad \dot{\boldsymbol{U}}(0, \boldsymbol{X}) = \dot{\boldsymbol{U}}_0(\boldsymbol{X}), \quad \ddot{\boldsymbol{U}}(0, \boldsymbol{X}) = \rho_0^{-1}\ \overline{\boldsymbol{B}}^{\mathrm{ext}}(0, \boldsymbol{X}), \tag{3.60}$$

and calculate all properties that are not time-dependent and set $n = 1$.

(S1) Update the times $t_n = n\ \triangle t$, $t_{n+1} = t_n + \triangle t$, and $t_{n+\frac{1}{2}} = \frac{1}{2}(t_n + t_{n+1})$. Enforce the velocity boundary condition $\dot{\boldsymbol{U}}_D(t, \boldsymbol{X})$ for points with prescribed velocites:

$$\dot{\boldsymbol{U}}\left(t_{n+\frac{1}{2}}, \boldsymbol{X}\right) = \dot{\boldsymbol{U}}(t_n, \boldsymbol{X}) + \frac{1}{2}\ \triangle t\ \ddot{\boldsymbol{U}}(t_n, \boldsymbol{X}), \qquad \forall \boldsymbol{X} \in \mathcal{B}_0^N \setminus \partial_{\mathrm{D}}\mathcal{B}_0 \tag{3.61}$$

$$\dot{\boldsymbol{U}}\left(t_{n+\frac{1}{2}}, \boldsymbol{X}\right) = \dot{\boldsymbol{U}}_{\mathrm{D}}\left(t_{n+\frac{1}{2}}, \boldsymbol{X}\right), \qquad \forall \boldsymbol{X} \in \mathcal{B}_0^N \cap \partial_{\mathrm{D}}\mathcal{B}_0. \tag{3.62}$$

(S2) Update the point displacements and positions

$$\boldsymbol{U}(t_{n+1},\boldsymbol{X}) = \boldsymbol{U}(t_n,\boldsymbol{X}) + \triangle t\ \dot{\boldsymbol{U}}(t_{n+\frac{1}{2}},\boldsymbol{X}), \tag{3.63}$$

$$\boldsymbol{x}(t_{n+1},\boldsymbol{X}) = \boldsymbol{X} + \boldsymbol{U}(t_{n+1},\boldsymbol{X}). \tag{3.64}$$

(S3) Evaluate $\overline{\boldsymbol{B}}^{\text{int}}$ for $\boldsymbol{U}(t_{n+1})$ and enforce the Neumann boundary condition $\overline{\boldsymbol{B}}_{\text{N}}(t,\boldsymbol{X})$ for points with prescribed external forces

$$\overline{\boldsymbol{B}}^{\text{ext}}(t_{n+1},\boldsymbol{X}) = \boldsymbol{0}, \qquad \forall \boldsymbol{X} \in \mathcal{B}_0^N \setminus \partial_{\text{N}}\mathcal{B}_0 \tag{3.65}$$

$$\overline{\boldsymbol{B}}^{\text{ext}}(t_{n+1},\boldsymbol{X}) = \overline{\boldsymbol{B}}_{\text{N}}(t_{n+1},\boldsymbol{X}), \qquad \forall \boldsymbol{X} \in \mathcal{B}_0^N \cap \partial_{\text{N}}\mathcal{B}_0. \tag{3.66}$$

Update the acceleration

$$\ddot{\boldsymbol{U}}(t_{n+1},\boldsymbol{X}) = \varrho_0^{-1}\left(\overline{\boldsymbol{B}}^{\text{int}}(t_{n+1},\boldsymbol{X}) + \overline{\boldsymbol{B}}^{\text{ext}}(t_{n+1},\boldsymbol{X})\right). \tag{3.67}$$

(S4) Update the velocity

$$\dot{\boldsymbol{U}}(t_{n+1},\boldsymbol{X}) = \dot{\boldsymbol{U}}\left(t_{n+\frac{1}{2}},\boldsymbol{X}\right) + \frac{1}{2}\triangle t\ \ddot{\boldsymbol{U}}(t_{n+1},\boldsymbol{X}). \tag{3.68}$$

(S5) Set $n := n+1$ and if $t_n < T$, go to step (S1).

The Velocity-Verlet algorithm is advantageous due to its simplicity, efficiency, and energy conservation properties. Additionally, it conserves wave propagation characteristics very well, which is especially important in dynamic fracture simulations [26]. In the context of peridynamics, it has been shown to perform well for dynamic problems involving fracture under large deformations.

3.8 | Temporal discretization with Jacobian-free Newton–Krylov

For quasi-static problems where accuracy is more important than computational speed, or when dealing with highly nonlinear material behavior, implicit solvers can provide superior performance. Unlike explicit methods, implicit methods solve for equilibrium at each load step by iteratively minimizing the residual force. The Newton-Raphson method is a widely used implicit solver for nonlinear problems, but it requires the assembly and factorization of the global Jacobian matrix, which can be computationally expensive and memory-intensive, especially for large-scale peridynamic simulations. The Jacobian-free Newton-Krylov (JFNK) method [21] is an implicit iterative solver particularly well-suited for quasi-static simulations with complex constitutive models, as it avoids the explicit formation of the Jacobian matrix.

The *global displacement field* $\underline{\boldsymbol{U}} : [0,\infty) \to \mathbb{R}^M$ represents the displacement of all discrete points in the body at time t. Here, $M = d\ N$ denotes the total number of degrees of freedom, with d being the spatial dimension and N the number of discrete points. The Newton-Raphson and also the JFNK method seeks the displacement field $\underline{\boldsymbol{U}}$ that satisfies the equilibrium condition

$$\underline{\boldsymbol{r}}(\underline{\boldsymbol{U}}) = \boldsymbol{0} \tag{3.69}$$

where the *global residual vector* $\underline{\boldsymbol{r}} : \mathbb{R}^M \to \mathbb{R}^M$ represents the out-of-balance force for all degrees of freedom in the discretized system. The global residual vector is assembled from point-wise residuals, where for a point $\boldsymbol{X}$, the *point residual* $\boldsymbol{r} : [0,\infty) \times \mathcal{B}_0 \to \mathbb{R}^d$ is defined as

$$\boldsymbol{r}(t,\boldsymbol{X}) = \left(\overline{\boldsymbol{B}}^{\text{int}}(t,\boldsymbol{X}) + \overline{\boldsymbol{B}}^{\text{ext}}(t,\boldsymbol{X})\right)V, \tag{3.70}$$

with the internal and external body force densities $\overline{\boldsymbol{B}}^{\text{int}}$ and $\overline{\boldsymbol{B}}^{\text{ext}}$, and the point volume $V(\boldsymbol{X})$.

Starting from an initial guess $\underline{\boldsymbol{U}}(0)$, Newton's method iteratively updates the displacement by solving the linearized system

$$\underline{\boldsymbol{J}}\,\underline{\boldsymbol{\Delta U}} = -\underline{\boldsymbol{r}}, \tag{3.71}$$

where $\underline{\boldsymbol{J}} \in \mathbb{R}^{M\times M}$ denotes the *Jacobian matrix*, which is also called the tangent stiffness matrix. The *global displacement increment* $\underline{\boldsymbol{\Delta U}} \in \mathbb{R}^M$ is the solution of the linear system. For each point $\boldsymbol{X}$, the displacement increment $\boldsymbol{\Delta U} \in \mathbb{R}^d$ is extracted from $\underline{\boldsymbol{\Delta U}}$, and the displacement is updated as

$$\boldsymbol{U}(t_n, \boldsymbol{X}) = \boldsymbol{U}(t_n, \boldsymbol{X}) + \boldsymbol{\Delta U}. \tag{3.72}$$

The iteration continues until the residual norm falls below a specified *convergence tolerance* $\tau \in \mathbb{R}^+$, that is, $\|\underline{\boldsymbol{r}}\| < \tau$, where $\|\bullet\|$ denotes the Euclidean norm.

In the JFNK method, the linear system in Equation (3.71) is solved using a Krylov subspace method, such as the Generalized Minimal Residual (GMRES) method [29]. Krylov methods iteratively build a solution by constructing an orthonormal basis of the Krylov subspace $\mathcal{K}_m = \text{span}\{\boldsymbol{w}, \underline{\boldsymbol{J}}\,\boldsymbol{w}, \underline{\boldsymbol{J}}^2\boldsymbol{w}, \ldots, \underline{\boldsymbol{J}}^{m-1}\boldsymbol{w}\}$. The key insight is that this construction only requires matrix-vector products of the form $\underline{\boldsymbol{J}}\,\boldsymbol{w}$, where $\boldsymbol{w} \in \mathbb{R}^M$ is an arbitrary direction vector generated internally by GMRES. Consequently, the full Jacobian matrix never needs to be assembled or stored.

This is particularly advantageous for peridynamic formulations, where the Jacobian matrix is often not available in analytical form due to the complexity of the constitutive models. The Jacobian-vector product can instead be approximated using central finite differences as

$$\underline{\boldsymbol{J}}\,\boldsymbol{w} \approx \frac{\underline{\boldsymbol{r}}(\underline{\boldsymbol{U}}(t_n) + \epsilon\,\boldsymbol{w}) - \underline{\boldsymbol{r}}(\underline{\boldsymbol{U}}(t_n) - \epsilon\,\boldsymbol{w})}{2\,\epsilon}. \tag{3.73}$$

This approximation requires only two additional residual evaluations per product, perturbing the displacement field in the direction $\boldsymbol{w}$ by a small amount ϵ. The *perturbation parameter* $\epsilon \in \mathbb{R}^+$ is computed adaptively to balance truncation error (which decreases with smaller ϵ) and floating-point roundoff error (which increases with smaller ϵ). A common heuristic for central differences is

$$\epsilon := \epsilon_s \sqrt[3]{\epsilon_{\text{mach}}}\,\frac{\|\underline{\boldsymbol{U}}\| + 1}{\|\boldsymbol{w}\|}, \tag{3.74}$$

where $\epsilon_s \in \mathbb{R}^+$ is a scaling factor typically set to $\epsilon_s = 1$, and ϵ_{mach} denotes the machine precision. This matrix-free approach reduces the memory requirement from $\mathcal{O}(M^2)$ for storing the full Jacobian to $\mathcal{O}(M)$, enabling simulations with large numbers of points.

The JFNK algorithm for quasi-static peridynamic simulations proceeds as follows:

(S0) Set the initial displacement as $\boldsymbol{U}(0, \boldsymbol{X}) = \boldsymbol{U}_0(\boldsymbol{X})$ and set $n = 1$.

(S1) Update the time $t_n = n\ \triangle\ t$ and the *load factor* $\beta_n = n/N_T \in [0, 1]$. Enforce the Dirichlet boundary condition $\boldsymbol{U}_{\text{D}}(\boldsymbol{X})$ and Neumann boundary condition $\overline{\boldsymbol{B}}_{\text{N}}(\boldsymbol{X})$ incrementally according to the load factor β_n

$$\boldsymbol{U}(t_n, \boldsymbol{X}) = \beta_n\,\boldsymbol{U}_{\text{D}}(\boldsymbol{X}), \qquad \forall \boldsymbol{X} \in \mathcal{B}_0^N \cap \partial_{\text{D}}\mathcal{B}_0 \tag{3.75}$$

$$\overline{\boldsymbol{B}}^{\text{ext}}(t_n, \boldsymbol{X}) = \beta_n\,\overline{\boldsymbol{B}}_{\text{N}}(\boldsymbol{X}), \qquad \forall \boldsymbol{X} \in \mathcal{B}_0^N \cap \partial_{\text{N}}\mathcal{B}_0. \tag{3.76}$$

Initialize the displacement for unconstrained points as

$$\boldsymbol{U}(t_n, \boldsymbol{X}) = \boldsymbol{U}(t_{n-1}, \boldsymbol{X}), \quad \forall \boldsymbol{X} \in \mathcal{B}_0^N \setminus \partial_{\text{D}}\mathcal{B}_0. \tag{3.77}$$

(S2) Evaluate $\overline{\boldsymbol{B}}^{\text{int}}$ for the current displacement field and compute the residual vector $\boldsymbol{r}$ for all points as

$$\boldsymbol{r}(t_n, \boldsymbol{X}) = \left(\overline{\boldsymbol{B}}^{\text{int}}(t_n, \boldsymbol{X}) + \overline{\boldsymbol{B}}^{\text{ext}}(t_n, \boldsymbol{X})\right) V_k, \qquad \forall \boldsymbol{X} \in \mathcal{B}_0^N \setminus \partial_{\text{D}}\mathcal{B}_0 \tag{3.78}$$

$$\boldsymbol{r}(t_n, \boldsymbol{X}) = \boldsymbol{0}, \qquad \forall \boldsymbol{X} \in \mathcal{B}_0^N \cap \partial_{\text{D}}\mathcal{B}_0. \tag{3.79}$$

If $\|\underline{\boldsymbol{r}}\| < \tau$, convergence is achieved and it can be proceeded with step (S4). Otherwise go to step (S3).

(S3) Solve the linear system $\underline{\underline{J}}\,\underline{\Delta \boldsymbol{U}} = -\underline{\boldsymbol{r}}$ using GMRES with matrix-free Jacobian–vector products. Update the displacement field and position as

$$\boldsymbol{U}(t_n, \boldsymbol{X}) = \boldsymbol{U}(t_n, \boldsymbol{X}) + \Delta \boldsymbol{U}, \tag{3.80}$$

$$\boldsymbol{x}(t_n, \boldsymbol{X}) = \boldsymbol{X} + \boldsymbol{U}(t_n, \boldsymbol{X}). \tag{3.81}$$

Then go back to step (S2).

(S4) Set $n := n + 1$ and if $n \leq N_T$, go to step (S1).

Note that the JFNK method requires more computational effort per load step compared to explicit methods, as multiple residual evaluations are needed for each GMRES iteration. However, the method is unconditionally stable and can handle large load steps, making it efficient for quasi-static problems where the dynamic response is not of interest. The convergence of this method is typically quadratic once the iterates are sufficiently close to the solution, provided the Jacobian is nonsingular and the initial guess is reasonable.

4 | STABILITY ISSUES AND BOND-ASSOCIATED MODELING

While peridynamics offers significant advantages for modeling discontinuities and complex fracture phenomena, various formulations face persistent numerical challenges that can compromise the accuracy and robustness of simulations. The correspondence formulation, despite its flexibility in incorporating classical constitutive models, introduces numerical instabilities such as zero-energy modes [7]. These are similar to hourglass modes known from finite element methods [4, 10, 28].

Bond-associated modeling approaches have emerged as a promising framework to overcome these challenges by modifying how material interactions are computed within the peridynamic theory. Rather than relying solely on point-wise averaging as in standard correspondence formulations, bond-associated methods incorporate bond-wise properties to stabilize the approximation of kinematic quantities such as the deformation gradient. Chen and Spencer [7] proposed an approach utilizing a different integration domain for each bond. Bazilevs et al. [1] introduced a bond-wise averaging of the deformation gradient, which has similarities to nodal integration techniques applied at the bond level. These approaches aim to eliminate unstable deformation modes while maintaining the fundamental nonlocal character of peridynamic interactions.

4.1 | Zero-energy modes and stabilization techniques

To illustrate zero-energy modes, consider an oscillatory displacement field $\boldsymbol{U}_{\text{zem}} : \mathcal{B}_0 \to \mathbb{R}^3$ over the body $\mathcal{B}_0$. The field $\boldsymbol{U}_{\text{zem}}$ is a zero-energy mode if it leads to an approximated deformation gradient

$$\overline{\boldsymbol{F}}(t, \boldsymbol{X})\Big|_{\boldsymbol{U}=\boldsymbol{U}_{\text{zem}}} = \boldsymbol{I}, \tag{4.1}$$

resulting in

$$\overline{\Psi}(t, \boldsymbol{X})\Big|_{\boldsymbol{U}=\boldsymbol{U}_{\text{zem}}} = 0, \tag{4.2}$$

and therefore zero strain energy density throughout the body. This field is usually characterized by high-frequency oscillations of the displacement values between neighboring points. Additionally, from Equation (4.1) and (4.2), it follows that the force vector state also vanishes, that is,

$$\boldsymbol{t}(t, \boldsymbol{X}, \boldsymbol{X}')\Big|_{\boldsymbol{U}=\boldsymbol{U}_{\text{zem}}} = \boldsymbol{0}. \tag{4.3}$$

Some literature states that these issues are related to the meshless discretization [5, 13], while Silling views them as a material instability rather than a numerical instability [31]. Silling derived a stability condition for the correspondence formulation based on the second variation of the strain energy density. Accordingly, the correspondence formulation is

stable if the condition

$$\int_{\mathcal{B}_0} \int_{\mathcal{H}(\boldsymbol{X})} \omega(\Delta \boldsymbol{X})(\mathrm{d}(\Delta \boldsymbol{x}) \cdot \mathrm{d}\boldsymbol{t})\, \mathrm{d}V'\, \mathrm{d}V > 0 \tag{4.4}$$

is satisfied for all small increments $\mathrm{d}(\Delta \boldsymbol{x})$ and $\mathrm{d}\boldsymbol{t}$ of the bond and the force vector state, respectively [31]. In the local form, this condition can be expressed as

$$\int_{\mathcal{H}(\boldsymbol{X})} \omega(\Delta \boldsymbol{X})(\mathrm{d}(\Delta \boldsymbol{x}) \cdot \mathrm{d}\boldsymbol{t})\, \mathrm{d}V' > 0 \qquad \forall \boldsymbol{X} \in \mathcal{B}_0. \tag{4.5}$$

To establish a connection between this stability condition and the zero-energy modes, consider a small increment $\mathrm{d}(\Delta \boldsymbol{x})$ due to a displacement field $\boldsymbol{U}_{\mathrm{zem}}$. With Equation (4.3), the corresponding increment of the force vector state results in

$$\mathrm{d}\boldsymbol{t}\Big|_{\boldsymbol{U}=\boldsymbol{U}_{\mathrm{zem}}} = \boldsymbol{0}, \tag{4.6}$$

harming the stability condition of Silling stated above.

However, the stability of the correspondence formulation is also influenced by the underlying local constitutive model. According to [31], from the stability condition, it follows that the local constitutive model must satisfy the condition

$$\mathrm{d}\boldsymbol{P} \cdot \mathrm{d}\overline{\boldsymbol{F}} > 0, \tag{4.7}$$

with an increment of the first Piola–Kirchhoff stress tensor $\mathrm{d}\boldsymbol{P}$ and an increment of the approximated deformation gradient $\mathrm{d}\overline{\boldsymbol{F}}$ for all deformations other than rigid rotations. Consider an oscillatory displacement field $\boldsymbol{U}_{\mathrm{zem}}$ such that

$$\omega(\Delta \boldsymbol{X})\ \mathrm{d}(\Delta \boldsymbol{x}) = \omega(-\Delta \boldsymbol{X})\ \mathrm{d}(-\Delta \boldsymbol{x}) \qquad \forall \boldsymbol{X} \in \mathcal{B}_0,\ \forall \boldsymbol{X}' \in \mathcal{H}(\boldsymbol{X}). \tag{4.8}$$

This leads with Equation (3.34) to

$$\mathrm{d}\overline{\boldsymbol{F}} = \boldsymbol{0}, \tag{4.9}$$

showing that the stability conditions of Silling are not satisfied.

To improve simulation results of the correspondence formulation, a stabilization term $\boldsymbol{t}^{\mathrm{zem}} : [0, \infty) \times \mathcal{B}_0 \times \mathcal{B}_0 \to \mathbb{R}^3$ is added to the force vector state in Equation (3.39), resulting in

$$\boldsymbol{t}(t, \boldsymbol{X}, \boldsymbol{X}') = \omega(\Delta \boldsymbol{X})\ \boldsymbol{P}(t, \boldsymbol{X})\ \boldsymbol{K}^{-1}(\boldsymbol{X}) \Delta \boldsymbol{X}(\boldsymbol{X}, \boldsymbol{X}') + \boldsymbol{t}^{\mathrm{zem}}(t, \boldsymbol{X}, \boldsymbol{X}'). \tag{4.10}$$

Several approaches to stabilize the correspondence formulation exist [8, 31, 39], differing in the way the stabilization term is defined. We want to focus on the two most common approaches, the one proposed by Silling [31] and the one proposed by Wan et al. [39].

The stabilization scheme of Silling [31] defines the stabilization term $\boldsymbol{t}^{\mathrm{zem}}$ as penalty force density

$$\boldsymbol{t}^{\mathrm{zem}}(t, \boldsymbol{X}, \boldsymbol{X}') = \frac{\omega(\Delta \boldsymbol{X})}{\omega_0(\boldsymbol{X})}\ C_s\ C_b(\Delta \boldsymbol{x} - \overline{\boldsymbol{F}}(t, \boldsymbol{X})\ \Delta \boldsymbol{X}), \tag{4.11}$$

with the bond constant C_b in Equation (3.11), a control parameter C_s and the *kernel integral* $\omega_0 : \mathcal{B}_0 \to \mathbb{R}^+$ defined as

$$\omega_0(\boldsymbol{X}) = \int_{\mathcal{H}(\boldsymbol{X})} \omega(\Delta \boldsymbol{X})\, \mathrm{d}V'. \tag{4.12}$$

The control parameter C_s is a scalar value that determines the strength of the stabilization term. Its value clearly influences the stability of the simulation, but it is not easy to determine. The correspondence formulation together with the Silling stabilization scheme is called CS model in the following.

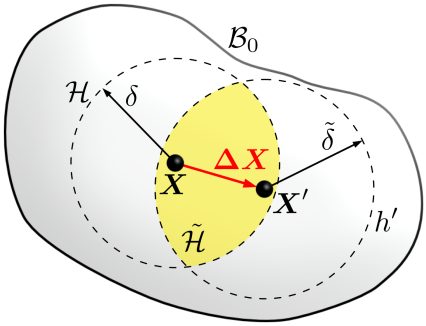

FIGURE 6 A peridynamic body $\mathcal{B}$ with bond-associated reaction zone $\tilde{\mathcal{H}}$ defined by the bond-horizon $\tilde{\delta}$.

Wan et al. [39] proposed a different stabilization scheme that eliminates the necessity of a control parameter. This scheme is based on the observation that the stabilization term should be proportional to the difference between the deformed and reference bond vectors. For the stabilization term $\boldsymbol{t}^{\text{zem}}$, Wan et al. [39] proposed the expression

$$\boldsymbol{t}^{\text{zem}}(t, \boldsymbol{X}, \boldsymbol{X}') = \omega(\Delta\boldsymbol{X})\, \boldsymbol{C}_1(\boldsymbol{X})(\Delta\boldsymbol{x} - \overline{\boldsymbol{F}}(t, \boldsymbol{X})\, \Delta\boldsymbol{X}). \tag{4.13}$$

The tensor $\boldsymbol{C}_1 : \mathcal{B}_0 \to \mathbb{R}^{3\times 3}$ is defined as

$$\boldsymbol{C}_1(\boldsymbol{X}) = \mathbb{C}\, \boldsymbol{K}^{-1}(\boldsymbol{X}), \tag{4.14}$$

with the fourth-order elastic modulus tensor $\mathbb{C}$ being derived from the elastic constants of the material. The correspondence formulation together with the Wan stabilization scheme is called CW model in the following.

The problem with all these stabilization schemes is that they do not effectively work for fracture simulations at finite deformations. The stabilization terms are not designed to handle the discontinuities and large deformations associated with fracture, which can lead to inaccurate results or even further instabilities. These challenges are discussed in detail in the following sections.

4.2 | Approach with bond-associated subdomain

Among the various bond-associated modeling approaches developed to address zero-energy modes, the method proposed by Chen and Spencer [7] represents one of the earliest and most widely recognized frameworks within the peridynamics community. Their approach fundamentally modifies the integration domain used for calculating the deformation gradient by introducing bond-specific subdomains, thereby moving away from the point-wise averaging that characterizes the standard correspondence formulation. This method has gained considerable attention in the literature and is often considered the canonical bond-associated model.

To eliminate zero-energy modes from the deformation state, Chen and Spencer [7] proposed an approach that calculates the deformation gradient with a bond-associated subdomain. First, a second neighborhood is introduced as

$$h'(\boldsymbol{X}') = \left\{\boldsymbol{X}'' \in \mathcal{B}_0 \mid 0 < \left|\boldsymbol{X}'' - \boldsymbol{X}'\right| \leq \tilde{\delta}\right\}, \tag{4.15}$$

which is the continuous infinite set of points inside the spherical neighborhood with radius $\tilde{\delta}$ around the point $\boldsymbol{X}'$, see Figure 6. Then, the bond-associated subdomain, also called *bond-associated reaction zone*, is defined as

$$\tilde{\mathcal{H}}(\boldsymbol{X}, \boldsymbol{X}') = \mathcal{H}(\boldsymbol{X}) \cap h'(\boldsymbol{X}'). \tag{4.16}$$

In terms of the correspondence formulation, the bond-associated shape tensor now can be calculated similar to Equation (3.31) as

$$\tilde{\boldsymbol{K}}(\boldsymbol{X}, \boldsymbol{X}') = \int_{\tilde{\mathcal{H}}(\boldsymbol{X}, \boldsymbol{X}')} \omega(\Delta\boldsymbol{X})\, \Delta\boldsymbol{X} \otimes \Delta\boldsymbol{X}\, \mathrm{d}V'. \tag{4.17}$$

With the bond-associated shape tensor, the bond-wise approximation of the deformation gradient yields

$$\tilde{\boldsymbol{F}}(t,\boldsymbol{X},\boldsymbol{X}') = \left(\int_{\tilde{\mathcal{H}}(\boldsymbol{X},\boldsymbol{X}')} \omega(\Delta\boldsymbol{X})\, \Delta\boldsymbol{x} \otimes \Delta\boldsymbol{X}\, \mathrm{d}V'\right) \tilde{\boldsymbol{K}}^{-1}(\boldsymbol{X},\boldsymbol{X}'). \tag{4.18}$$

With this, the bond-associated first Piola–Kirchhoff stress tensor can be calculated as

$$\tilde{\boldsymbol{P}}(t,\boldsymbol{X},\boldsymbol{X}') = \boldsymbol{P}(\tilde{\boldsymbol{F}}(t,\boldsymbol{X},\boldsymbol{X}')). \tag{4.19}$$

When calculating the force state, the different integration domains for each bond have to be considered, which leads to

$$\boldsymbol{t}(t,\boldsymbol{X},\boldsymbol{X}') = \frac{\int_{\tilde{\mathcal{H}}(\boldsymbol{X},\boldsymbol{X}')} \mathrm{d}V'}{\int_{\mathcal{H}(\boldsymbol{X})} \mathrm{d}V'}\, \omega(\Delta\boldsymbol{X})\, \tilde{\boldsymbol{P}}(t,\boldsymbol{X},\boldsymbol{X}')\, \tilde{\boldsymbol{K}}^{-1}(\boldsymbol{X},\boldsymbol{X}')\, \Delta\boldsymbol{X}. \tag{4.20}$$

When approximating the wave speed with this bond-associated approach, an error depending on the size of the second horizon $\tilde{\delta}$ is introduced. It can also be shown that some instabilities are still present in the bond-associated formulation [6, 8].

The stabilization mechanism of this approach differs fundamentally from the established stabilization methods described before. For zero-energy modes, the bond-associated subdomain $\tilde{\mathcal{H}}(\boldsymbol{X},\boldsymbol{X}')$ captures local deformation variations, ensuring that $\tilde{\boldsymbol{F}}(t,\boldsymbol{X},\boldsymbol{X}') \neq \boldsymbol{I}$ even when oscillatory displacements would yield $\overline{\boldsymbol{F}}(t,\boldsymbol{X}) = \boldsymbol{I}$ in the standard formulation. This provides nonzero force states $\mathrm{d}\boldsymbol{t} \neq \boldsymbol{0}$ that satisfy the stability condition in Equation (4.5).

Despite its theoretical appeal and widespread recognition in the peridynamics literature, the Chen and Spencer approach presents several practical challenges that limit its applicability for robust numerical simulations. The introduction of the bond horizon $\tilde{\delta}$ as an additional parameter creates complications in determining appropriate values, particularly for complex geometries or varying discretizations. Moreover, the persistence of certain instabilities, as documented in subsequent studies [6, 8], indicates that while this approach reduces zero-energy modes, it does not eliminate them entirely. Our implementation with this formulation encountered numerical difficulties that proved challenging to resolve. Consequently, while this approach is presented for completeness and to acknowledge its historical significance in bond-associated modeling, it is not employed in the numerical investigations presented in this work. Instead, the focus lies on the bond-associated quadrature point approach discussed in the following subsection, which has demonstrated superior stability and robustness in computational studies.

4.3 | Approach with bond-associated quadrature points

Behzadinasab et al. [1–3, 40] introduced a new way of bond-associated modeling, which uses bond-associated quadrature points. They proposed that the classical correspondence model can be understood as a discretization with nodal quadrature at every point. This is similar to reduced-order quadrature in the finite element method with only one Gaussian point per element. To overcome the instabilities, the higher-order quadrature can be achieved with quadrature points at the center of each bond, as illustrated in Figure 7. This bond-associated quadrature point (BAQP) approach has shown promising results in mitigating zero-energy modes and enhancing the stability of the correspondence formulation.

First, a bond-wise approximation of the deformation gradient is introduced as

$$\tilde{\boldsymbol{F}}(t,\boldsymbol{X},\boldsymbol{X}') = \tilde{\boldsymbol{F}}^{\mathrm{ave}}(t,\boldsymbol{X},\boldsymbol{X}') + \tilde{\boldsymbol{F}}^{\mathrm{cor}}(t,\boldsymbol{X},\boldsymbol{X}'), \tag{4.21}$$

where the average deformation gradient of a bond is calculated as

$$\tilde{\boldsymbol{F}}^{\mathrm{ave}}(t,\boldsymbol{X},\boldsymbol{X}') = \frac{1}{2}\left(\overline{\boldsymbol{F}}(t,\boldsymbol{X}) + \overline{\boldsymbol{F}}(t,\boldsymbol{X}')\right), \tag{4.22}$$

and a correction term as

$$\tilde{\boldsymbol{F}}^{\mathrm{cor}}(t,\boldsymbol{X},\boldsymbol{X}') = \left((\boldsymbol{x}'-\boldsymbol{x}) - \tilde{\boldsymbol{F}}^{\mathrm{ave}}(t,\boldsymbol{X},\boldsymbol{X}')(\boldsymbol{X}'-\boldsymbol{X})\right) \otimes \frac{(\boldsymbol{X}'-\boldsymbol{X})}{|(\boldsymbol{X}'-\boldsymbol{X})|^2}. \tag{4.23}$$

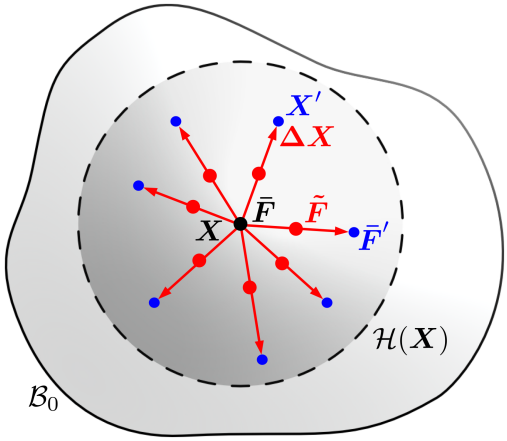

FIGURE 7 Higher-order quadrature with bond-associated quadrature points at the center of each bond.

The bond-associated deformation gradient $\tilde{\boldsymbol{F}}$ can be understood as the deformation gradient at the quadrature point in the middle of the bond.

With the bond-associated deformation gradient, the bond-associated strain energy density can be calculated as

$$\tilde{\Psi}(t,\boldsymbol{X},\boldsymbol{X}') = \Psi(\tilde{\boldsymbol{F}}(t,\boldsymbol{X},\boldsymbol{X}')). \tag{4.24}$$

Consequently, the strain energy density of a point can be approximated as the average of the strain energy densities of all bonds connected to that point with

$$\overline{\Psi}(t,\boldsymbol{X}) = \int_{\mathcal{H}(\boldsymbol{X})} \overline{\omega}_b(\boldsymbol{X},\boldsymbol{X}')\, \tilde{\Psi}(t,\boldsymbol{X},\boldsymbol{X}')\, \mathrm{d}V', \tag{4.25}$$

where the *averaged bond kernel function* $\overline{\omega}_b : \mathcal{B}_0 \times \mathcal{B}_0 \to \mathbb{R}^+$ is defined as

$$\overline{\omega}_b(\boldsymbol{X},\boldsymbol{X}') = \frac{1}{2}\left(\frac{\omega(\boldsymbol{X}'-\boldsymbol{X})}{\omega_0(\boldsymbol{X})} + \frac{\omega(\boldsymbol{X}-\boldsymbol{X}')}{\omega_0(\boldsymbol{X}')}\right), \tag{4.26}$$

with the *kernel integral* $\omega_0 : \mathcal{B}_0 \to \mathbb{R}^+$ defined as

$$\omega_0(\boldsymbol{X}) = \int_{\mathcal{H}(\boldsymbol{X})} \omega(\Delta\boldsymbol{X})\, \mathrm{d}V'. \tag{4.27}$$

Similarly, the first Piola–Kirchhoff stress tensor can be calculated for each bond as

$$\tilde{\boldsymbol{P}}(t,\boldsymbol{X},\boldsymbol{X}') = \boldsymbol{P}(\tilde{\boldsymbol{F}}(t,\boldsymbol{X},\boldsymbol{X}')). \tag{4.28}$$

Analogously to Equation (4.22), the force state can be calculated as

$$\boldsymbol{t}(t,\boldsymbol{X},\boldsymbol{X}') = \boldsymbol{t}^{\mathrm{ave}}(t,\boldsymbol{X},\boldsymbol{X}') + \boldsymbol{t}^{\mathrm{cor}}(t,\boldsymbol{X},\boldsymbol{X}'). \tag{4.29}$$

The average force state yields

$$\boldsymbol{t}^{\mathrm{ave}}(t,\boldsymbol{X},\boldsymbol{X}') = \left(\int_{\mathcal{H}(\boldsymbol{X})} \overline{\omega}_b(\boldsymbol{X},\boldsymbol{X}'')\, \tilde{\boldsymbol{P}}(t,\boldsymbol{X},\boldsymbol{X}'')\, \mathrm{d}V''\right)\frac{\boldsymbol{\Psi}(\boldsymbol{X},\boldsymbol{X}')}{V'}, \tag{4.30}$$

and the correction term

$$\boldsymbol{t}^{\mathrm{cor}}(t,\boldsymbol{X},\boldsymbol{X}') = \overline{\omega}_b(\boldsymbol{X},\boldsymbol{X}')\,\tilde{\boldsymbol{P}}(t,\boldsymbol{X},\boldsymbol{X}')\,\frac{(\boldsymbol{X}'-\boldsymbol{X})}{\left|(\boldsymbol{X}'-\boldsymbol{X})\right|^2} - \left(\int_{\mathcal{H}(\boldsymbol{X})} \overline{\omega}_b(\boldsymbol{X},\boldsymbol{X}'')\,\tilde{\boldsymbol{P}}(t,\boldsymbol{X},\boldsymbol{X}'')\,\frac{(\boldsymbol{X}''-\boldsymbol{X})\otimes(\boldsymbol{X}''-\boldsymbol{X})}{\left|(\boldsymbol{X}''-\boldsymbol{X})\right|^2}\,\mathrm{d}V''\right)\frac{\boldsymbol{\Psi}(\boldsymbol{X},\boldsymbol{X}')}{V'}. \tag{4.31}$$

These equations are also derived in detail in [40] and highlighted in [1]. The previous equations can be reformulated by introducing the *nonuniform stress tensor* $\boldsymbol{Z}: [0,\infty)\times\mathcal{B}_0 \to \mathbb{R}^{3\times3}$, defined as

$$\boldsymbol{Z}(t,\boldsymbol{X}) = \int_{\mathcal{H}(\boldsymbol{X})} \overline{\omega}_b(\boldsymbol{X},\boldsymbol{X}')\,\tilde{\boldsymbol{P}}(t,\boldsymbol{X},\boldsymbol{X}')\left(\boldsymbol{I} - \frac{\Delta\boldsymbol{X}\otimes\Delta\boldsymbol{X}}{|\Delta\boldsymbol{X}|^2}\right)\mathrm{d}V'. \tag{4.32}$$

With $\boldsymbol{Z}$, Equation (4.29) can be rewritten as

$$\boldsymbol{t}(t,\boldsymbol{X},\boldsymbol{X}') = \overline{\omega}_b(\boldsymbol{X},\boldsymbol{X}')\,\tilde{\boldsymbol{P}}(t,\boldsymbol{X},\boldsymbol{X}')\,\frac{\Delta\boldsymbol{X}}{|\Delta\boldsymbol{X}|} + \boldsymbol{Z}(t,\boldsymbol{X})\frac{\boldsymbol{\Psi}(\boldsymbol{X},\boldsymbol{X}')}{V'}. \tag{4.33}$$

In the context of this bond-associated modeling, the kernel function ω has to fulfill the normalization condition

$$\omega_0(\boldsymbol{X}) = 1 \qquad \forall\,\boldsymbol{X}\in\mathcal{B}_0. \tag{4.34}$$

Therefore, a cubic spline kernel function is

$$\omega(\Delta\boldsymbol{X}) = \frac{8}{\pi\delta^3}\cdot\begin{cases} 1-6\left(\frac{|\Delta\boldsymbol{X}|}{\delta}\right)^2+6\left(\frac{|\Delta\boldsymbol{X}|}{\delta}\right)^3 & \text{if } \frac{|\Delta\boldsymbol{X}|}{\delta}\le\frac{1}{2},\\ 2\left(1-\frac{|\Delta\boldsymbol{X}|}{\delta}\right)^3 & \text{if } \frac{1}{2}<\frac{|\Delta\boldsymbol{X}|}{\delta}\le 1,\\ 0 & \text{if } \frac{|\Delta\boldsymbol{X}|}{\delta}>1. \end{cases} \tag{4.35}$$

This formulation finally can be used for stable continuum consistent calculations of the correspondence formulation and is inherently free of zero-energy modes. However, the additional integrations over the neighborhood in Equation (4.30) and (4.31) increase the computational cost of this formulation by a factor in the order of ~ 3. Nevertheless, the increased stability and robustness of this bond-associated quadrature point approach make it a promising method for practical applications of the correspondence formulation in peridynamics.

4.4 | Zero-energy modes in a patch test

To illustrate zero-energy modes effectively, we consider a one-dimensional peridynamic body discretized with a uniform point spacing $\vartriangle x$ and equidistant material points X_n with $n\in\{1,2,3,4,5\}$, as shown in Figure 8. Note that in a one-dimensional setting, all properties reduce to scalar values. For a horizon $\delta > 2\vartriangle x$, the neighborhood of point X_3 includes $\mathcal{H}(X_3)=\{X_1,X_2,X_4,X_5\}$. With a constant kernel function $\omega(\Delta X)=1$ and uniform volumes $V_i = V$, the shape tensor for point X_3 is defined as

$$K(X_3) = \sum_{X_n\in\mathcal{H}(X_3)} \omega(X_n-X_3)\,(X_n-X_3)^2\,V = V\sum_{X_n\in\mathcal{H}(X_3)}(X_n-X_3)^2. \tag{4.36}$$

For the positions $X_1 = X_3 - 2\vartriangle x$, $X_2 = X_3 - \vartriangle x$, $X_4 = X_3 + \vartriangle x$, and $X_5 = X_3 + 2\vartriangle x$, this yields

$$K(X_3) = V\left[4\vartriangle x^2 + \vartriangle x^2 + \vartriangle x^2 + 4\vartriangle x^2\right] = 10\,V\vartriangle x^2. \tag{4.37}$$

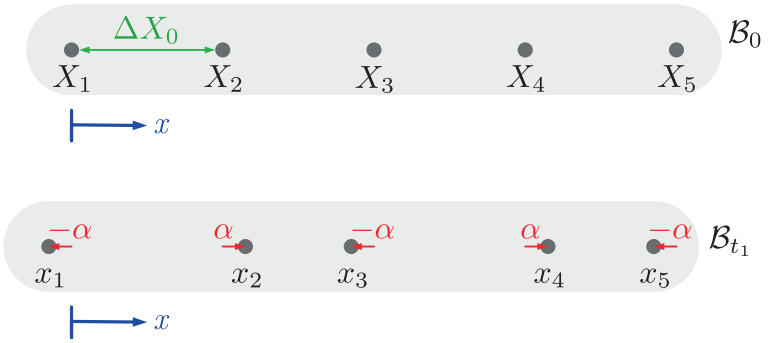

FIGURE 8 Example of a zero-energy mode displacement pattern in a discretized one-dimensional peridynamic model.

The point positions in the deformed state $\mathcal{B}_{t_1}$ at time t_1 are $x_n = X_n + U(t_1, X_n)$, where $U(t_1, X_n)$ represents the displacement. At this specific time t_1, we introduce an alternating displacement pattern given by

$$U_n = U(t_1, X_n) = (-1)^n \alpha, \tag{4.38}$$

as shown in Figure 8. According to Equation (3.34), the approximated deformation gradient for this deformation can be calculated for point X_3 as

$$\begin{aligned} \overline{F}(t, X_3) &= \left(\sum_{X_n \in \mathcal{H}(X_3)} \omega(X_n - X_3)\ (x_n - x_3)(X_n - X_3)\ V \right) K^{-1}(X_3) \\ &= \frac{V}{K(X_3)} \sum_{X_n \in \mathcal{H}(X_3)} (x_n - x_3)(X_n - X_3) \end{aligned} \tag{4.39}$$

For the initial state at time $t = 0$ with $U(0, X_n) = 0$, the approximated deformation gradient yields

$$\overline{F}(0, X_3) = \frac{V}{K(X_3)} \sum_{X_n \in \mathcal{H}(X_3)} (X_n - X_3)^2 = \frac{V}{K(X_3)} \cdot \frac{K(X_3)}{V} = 1, \tag{4.40}$$

which corresponds to the deformation gradient of an undeformed body. Substituting the current positions $x_n = X_n + U_n$ with the alternating deformation pattern defined in Equation (4.38) at time t_1 results in

$$\begin{aligned} \overline{F}(t_1, X_3) &= \frac{V}{K(X_3)} \sum_{X_n \in \mathcal{H}(X_3)} [(X_n - X_3) + (U_n - U_3)](X_n - X_3) \\ &= \frac{V}{K(X_3)} \left[\sum_{X_n \in \mathcal{H}(X_3)} (X_n - X_3)^2 + \sum_{X_n \in \mathcal{H}(X_3)} (U_n - U_3)(X_n - X_3) \right]. \end{aligned} \tag{4.41}$$

Inserting Equation (4.38) into the second term, we get

$$\sum_{X_n \in \mathcal{H}(X_3)} (U_n - U_3)(X_n - X_3) = -2\ \alpha\ \ \Delta x + 2\ \alpha\ \ \Delta x = 0. \tag{4.42}$$

Therefore, the approximated deformation gradient in Equation (4.41) evaluates to

$$\overline{F}(t_1, X_3) = \frac{V}{K(X_3)} \cdot \frac{K(X_3)}{V} = 1. \tag{4.43}$$

This demonstrates that despite the zigzag displacement pattern with alternating displacements in Equation (4.38), the approximated deformation gradient remains identical to that of an undeformed body.

Such deformation patterns with nontrivial displacement fields produce no change in the strain energy, which explains why these modes encounter no resistance in the correspondence formulation. These zero-energy modes pose serious stability challenges in numerical simulations, as they can grow unconstrained over time. In higher dimensions, zero-energy modes typically manifest as checkerboard patterns, where neighboring points move in alternating directions. Regardless of dimension, the fundamental issue remains: certain displacement patterns fail to generate strain energy in the correspondence formulation due to the averaging in the deformation gradient calculation.

To demonstrate this effect in a three-dimensional setting, a cubic domain with edge length $L = 1$ m is discretized with $40 \times 40 \times 40$ material points and a spacing of $\Delta x = 0.025$ m. The horizon is set to $\delta = 3.015 \ \Delta x$, and the material parameters are $E = 210000$ MPa, $\nu = 0.25$, and $\rho_0 = 8000$ kg/m^3. To avoid truncated neighborhoods at the domain boundaries, the simulation domain is extended by a buffer region of at least one horizon in each direction. A three-dimensional checkerboard displacement field is prescribed with the components

$$
\begin{aligned}
U_1(\boldsymbol{X}) &= A \cos\left(\frac{\pi X_2}{\Delta x}\right) \cos\left(\frac{\pi X_3}{\Delta x}\right), \\
U_2(\boldsymbol{X}) &= A \cos\left(\frac{\pi X_1}{\Delta x}\right) \cos\left(\frac{\pi X_3}{\Delta x}\right), \\
U_3(\boldsymbol{X}) &= A \cos\left(\frac{\pi X_1}{\Delta x}\right) \cos\left(\frac{\pi X_2}{\Delta x}\right),
\end{aligned} \tag{4.44}
$$

with the amplitude $A = 10^{-3} \ \Delta x$. Each displacement component varies sinusoidally with a wavelength of $\lambda = 2 \ \Delta x$ in the two transverse coordinate directions, producing an alternating sign pattern on the regular grid. Similar to the one-dimensional example, this displacement field constitutes a zero-energy mode for the standard correspondence formulation in the interior of the domain: the approximated deformation gradient remains $\overline{\boldsymbol{F}} = \boldsymbol{I}$ despite the nontrivial displacement, resulting in a strain energy density of zero. The simulation is performed by defining a prescribed displacement field and calculating the resulting strain energy density for different peridynamic formulations.

The results are shown in Figure 9. The CC model with a constant kernel $\omega(\boldsymbol{\Delta X}) = 1$ shows a strain energy density of zero in the interior of the domain. The CS and CW stabilized models also exhibit zero strain energy density in the interior. While these stabilization techniques add penalty forces to counteract zero-energy modes, the strain energy density is still computed from the approximated deformation gradient $\overline{\boldsymbol{F}}$, which remains equal to the identity tensor for this displacement pattern. Consequently, the penalty-based stabilization approaches do not affect the strain energy density.

In contrast, the BAQP model shows a nonzero strain energy density in the interior of the domain. The bond-based model with energy surface correction computes the strain energy from individual bond stretches, which are nonzero for the checkerboard displacement pattern. The BAQP model captures the oscillatory deformation through the bond-associated deformation gradient, where the correction term ensures that $\tilde{\boldsymbol{F}} \neq \boldsymbol{I}$ even when the point-level deformation gradient yields $\overline{\boldsymbol{F}} = \boldsymbol{I}$.

All models show deviations in the strain energy density near the boundaries of the domain. Despite the buffer region, the outermost points still have truncated neighborhoods, which affects the deformation gradient approximation. For the CC, CS, and CW models, the truncated neighborhoods break the symmetry that causes the odd-symmetric displacement contributions to cancel exactly in the deformation gradient calculation. As a result, $\overline{\boldsymbol{F}} \neq \boldsymbol{I}$ near the boundaries, leading to a nonzero strain energy density. For the BAQP model, the boundary deviations arise from the modified kernel normalization and bond contributions in truncated neighborhoods. For the BAQP model, the boundary effects are very small, confirming the robustness of the bond-associated quadrature approach also for inhomogeneous deformation fields.

4.5 | Large deformations and objectivity

To model large deformations using the correspondence formulation, the first Piola–Kirchhoff stress tensor must remain invariant under rigid body motions. Failure to ensure this invariance can lead to instabilities and the breakdown of simulations. Objectivity requires that the material response remains unchanged under superposed rigid body motions. One approach to enforce objectivity in numerical simulations is the algorithm proposed by Flanagan and Taylor [9], which has gained significant attention in the context of peridynamics. Their method introduces a rotation tensor to explicitly account for rigid body motions, and the stress contributions are calculated incrementally using an unrotated rate of deformation tensor.

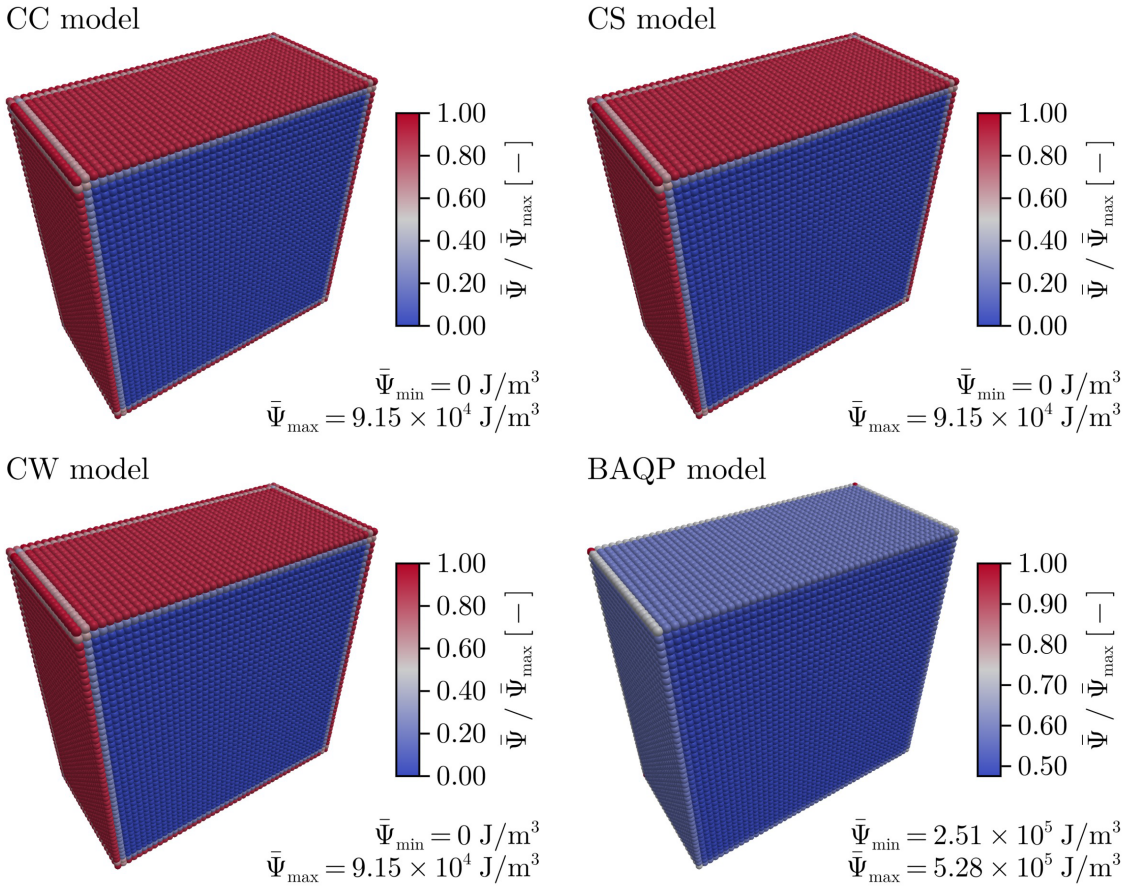

FIGURE 9 Strain energy density for the 3D checkerboard displacement field, showing results for the CC model with a constant kernel (top left), the CS and CW stabilized models with constant kernel (top right and bottom left), and the BAQP model (bottom right). The domain is cut in half at $X_1 = 0$.

To use the objectivity enforcement of the Flanagan & Taylor algorithm in the context of the correspondence formulation, a few definitions are needed. First, the spatial velocity gradient $\boldsymbol{l}$ is decomposed into its symmetric and antisymmetric parts, the rate of deformation tensor $\boldsymbol{d}$ and the spin tensor $\boldsymbol{w}$, respectively. The polar decomposition of the deformation gradient $\overline{\boldsymbol{F}}$ leads to the relation

$$\overline{\boldsymbol{F}}(t, \boldsymbol{X}) = \boldsymbol{v}(t, \boldsymbol{X})\ \boldsymbol{R}(t, \boldsymbol{X}), \tag{4.45}$$

with the left stretch tensor $\boldsymbol{v} : [0, \infty) \times \mathcal{B}_0 \to \mathbb{R}^{3\times3}$ and the rotation tensor $\boldsymbol{R} : [0, \infty) \times \mathcal{B}_0 \to \mathrm{SO}(3)$. Please note that the left stretch tensor $\boldsymbol{v}$ should not be confused with the velocity. With $\boldsymbol{v}$, the tensor $\boldsymbol{\Omega} : [0, \infty) \times \mathcal{B}_0 \to \mathbb{R}^{3\times3}$ is defined as

$$\Omega_{ij}(t, X_i) = e_{ikj}\ q_k(t, X_i), \tag{4.46}$$

with the Levi-Civita symbol e_{ijk} and the tensor

$$\boldsymbol{q}(t, \boldsymbol{X}) = \boldsymbol{p}(t, \boldsymbol{X}) + [\mathrm{tr}(\boldsymbol{v}(t, \boldsymbol{X}))\ \boldsymbol{I} - \boldsymbol{v}(t, \boldsymbol{X})]^{-1} \boldsymbol{z}(t, \boldsymbol{X}), \tag{4.47}$$

with

$$p_i(t, X_i) = -\frac{1}{2} e_{ijk} w_{jk}(t, X_i), \qquad z_i(t, X_i) = e_{ikj}\ d_{jm}(t, X_i)\ v_{mk}(t, X_i). \tag{4.48}$$

The expression $\boldsymbol{\Omega}$ is used to calculate the orthogonal tensor $\boldsymbol{Q} : [0, \infty) \times \mathcal{B}_0 \to \mathbb{R}^{3\times3}$ as

$$\boldsymbol{Q}(t, \boldsymbol{X}) = \boldsymbol{I} + \sin(\triangle\ t\ \Omega(t, \boldsymbol{X})) \frac{\boldsymbol{\Omega}(t, \boldsymbol{X})}{\Omega(t, \boldsymbol{X})} - (1 - \cos(\triangle\ t\ \Omega(t, \boldsymbol{X}))) \frac{\boldsymbol{\Omega}^2(t, \boldsymbol{X})}{\Omega^2(t, \boldsymbol{X})}, \tag{4.49}$$

with the scalar valued function $\Omega(t,\boldsymbol{X}) = \sqrt{\boldsymbol{q}(t,\boldsymbol{X}) \cdot \boldsymbol{q}(t,\boldsymbol{X})}$. The rotation tensor $\boldsymbol{R}$ then can be calculated incrementally with the results of the previous time step $\triangle\, t$ as

$$\boldsymbol{R}(t+\triangle\, t,\boldsymbol{X}) = \boldsymbol{Q}(t,\boldsymbol{X})\ \boldsymbol{R}(t,\boldsymbol{X}). \tag{4.50}$$

The rate of change of the left-stretch tensor yields

$$\dot{\boldsymbol{v}}(t,\boldsymbol{X}) = \boldsymbol{l}(t,\boldsymbol{X})\ \boldsymbol{v}(t,\boldsymbol{X}) - \boldsymbol{v}(t,\boldsymbol{X})\ \boldsymbol{\Omega}(t,\boldsymbol{X}) + \mathcal{O}(|\boldsymbol{\Delta X}|^2), \tag{4.51}$$

which then is used to update the left-stretch tensor by

$$\boldsymbol{v}(t+\triangle\, t,\boldsymbol{X}) = \boldsymbol{v}(t,\boldsymbol{X}) + \dot{\boldsymbol{v}}(t,\boldsymbol{X})\ \triangle\, t. \tag{4.52}$$

Finally, the unrotated rate of deformation tensor $\tilde{\boldsymbol{d}}$ can be calculated as

$$\tilde{\boldsymbol{d}}(t+\triangle\, t,\boldsymbol{X}) = \boldsymbol{R}^{\mathrm{T}}(t+\triangle\, t,\boldsymbol{X})\ \overline{\boldsymbol{d}}(t+\triangle\, t,\boldsymbol{X})\ \boldsymbol{R}(t+\triangle\, t,\boldsymbol{X}), \tag{4.53}$$

with the approximated rate of deformation tensor $\overline{\boldsymbol{d}} = \boldsymbol{d}(\overline{\boldsymbol{F}})$ in Equation (2.41).

The actual objectivity enforcement is now achieved by rotating the stress tensor with the rotation tensor $\boldsymbol{R}$, and also by calculating the stress contributions incrementally. For example for a linear elastic material, the unrotated stress tensor $\tilde{\boldsymbol{\sigma}}$ can be updated by

$$\tilde{\boldsymbol{\sigma}}(t+\triangle\, t,\boldsymbol{X}) = \tilde{\boldsymbol{\sigma}}(t,\boldsymbol{X}) + 2\ G\ \boldsymbol{\Delta\varepsilon}^{\mathrm{dev}} + K\ \mathrm{tr}\boldsymbol{\Delta\varepsilon}\ \boldsymbol{I}, \tag{4.54}$$

with the shear modulus G, the bulk modulus K, and the strain increments

$$\boldsymbol{\Delta\varepsilon} = \triangle\, t\ \tilde{\boldsymbol{d}}(t+\triangle\, t,\boldsymbol{X}), \qquad \boldsymbol{\Delta\varepsilon}^{\mathrm{dev}} = \boldsymbol{\Delta\varepsilon} - \frac{1}{3}\mathrm{tr}\boldsymbol{\Delta\varepsilon}\ \boldsymbol{I}. \tag{4.55}$$

The rotated stress tensor $\boldsymbol{\sigma}$ is given by

$$\boldsymbol{\sigma}(t+\triangle\, t,\boldsymbol{X}) = \boldsymbol{R}(t+\triangle\, t,\boldsymbol{X})\ \tilde{\boldsymbol{\sigma}}(t+\triangle\, t,\boldsymbol{X})\ \boldsymbol{R}^{\mathrm{T}}(t+\triangle\, t,\boldsymbol{X}). \tag{4.56}$$

Now, the first Piola–Kirchhoff stress tensor used in Equation (3.42) is calculated as

$$\boldsymbol{P}(t+\triangle\, t,\boldsymbol{X}) = J(t+\triangle\, t,\boldsymbol{X})\ \boldsymbol{\sigma}(t+\triangle\, t,\boldsymbol{X})\ \boldsymbol{F}^{-\mathrm{T}}(t+\triangle\, t,\boldsymbol{X}), \tag{4.57}$$

with the Jacobian J and the deformation gradient $\boldsymbol{F}$.

To investigate the practical relevance of the objectivity enforcement and the influence of zero-energy modes under large deformations, two numerical examples are presented. First, a bar of the dimensions $0.1L \times 0.1L \times L$ with length $L = 1$ m is considered. The bar extends along the X_3-axis and is uniformly discretized with $N_{xy} = 30$ points along each transverse direction and a point spacing of $\triangle\, x = 0.1L/N_{xy}$. The horizon is set to $\delta = 3.015\ \ \triangle\, x$. The bar is subjected to an initial velocity field that induces a twisting motion around its longitudinal axis. The initial velocity depends on the material point position $\boldsymbol{X} = [X_1, X_2, X_3]^{\mathrm{T}}$ and is defined as

$$\dot{\boldsymbol{U}}_0(\boldsymbol{X}) = \varphi_0\ \alpha(\boldsymbol{X})\ r(\boldsymbol{X}) \begin{bmatrix} \sin(\theta(\boldsymbol{X}) + \pi) \\ -\cos(\theta(\boldsymbol{X}) + \pi) \\ 0 \end{bmatrix}, \tag{4.58}$$

with the angular velocity magnitude $\varphi_0 = 150$ Hz, the radial distance from the center of the bar $r(\boldsymbol{X}) = \sqrt{X_1^2 + X_2^2}$, and the angle $\theta(\boldsymbol{X}) = \arctan\left(\frac{X_2}{X_1}\right)$. The smooth modulation function

$$\alpha(\boldsymbol{X}) = \sin\left(\frac{\pi}{2\,L}\left(X_3 + \frac{L}{2} - 3.01\ \ \triangle\, x\right)\right) \tag{4.59}$$

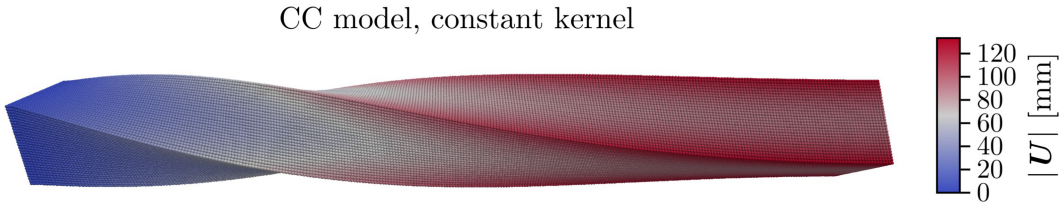

FIGURE 10 Large rotations in a twisting bar using the CC model with constant kernel function and without objectivity enforcement.

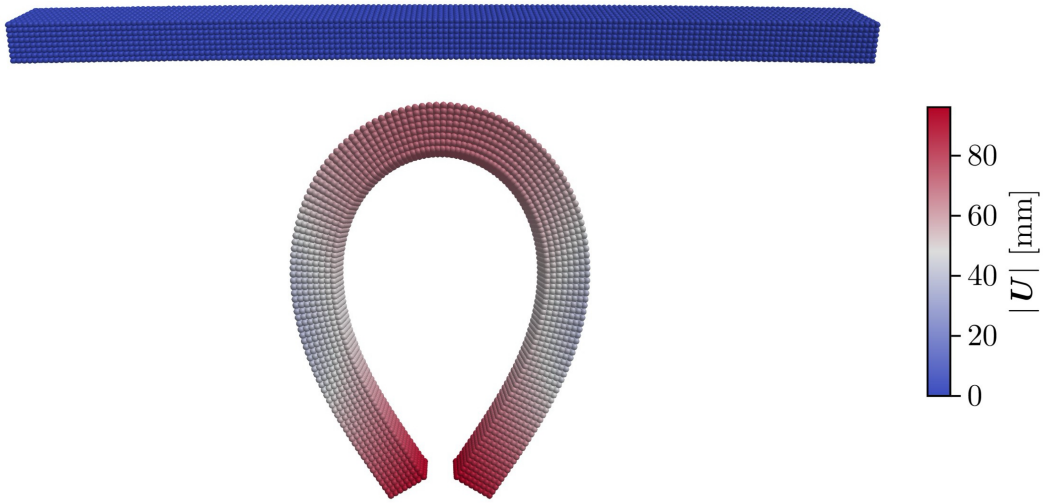

FIGURE 11 Bending of a bar using the CC model and a constant kernel with initial configuration (top) and final deformed configuration (bottom).

ensures that the velocity field vanishes smoothly near one end of the bar, so that the bar is fixed at one end and twists freely at the other. The material is modeled using a hyperelastic Saint Venant–Kirchhoff model formulated in terms of the right Cauchy–Green tensor $\boldsymbol{C}$. The simulation is performed with the CC model using the *constant kernel* function $\omega(\boldsymbol{\Delta X}) = 1$.

The result is shown in Figure 10. The bar undergoes large rotations along its longitudinal axis and the simulation remains stable throughout. Although the CC model with a constant kernel is known to be susceptible to zero-energy modes, no instabilities are visible in this example. This indicates that for large deformations involving smooth displacement fields, zero-energy modes are not the primary concern. Furthermore, the objectivity enforcement of the Flanagan & Taylor algorithm is not needed here, since the hyperelastic material law is formulated in terms of the right Cauchy–Green tensor $\boldsymbol{C}$, which is objective by construction. Results obtained with the BAQP model are quantitatively similar to those of the CC model and are therefore not shown.

As a second example, the bending of a bar is considered. The bar has a length of $L_x = 0.2$ m and a square cross section with side length $L_{yz} = 0.01$ m. It is uniformly discretized with $N_{yz} = 8$ points along each transverse direction, yielding a point spacing of $\vartriangle x = L_{yz}/N_{yz} = 1.25 \times 10^{-3}$ m. The horizon is set to $\delta = 5.15 \ \vartriangle x$. The material parameters are a density of $\varrho_0 = 1600$ kg/m^3, Young's modulus $E = 2.3$ GPa, and Poisson's ratio $\nu = 0.25$. The bar has a small initial curvature to trigger bending rather than pure compression. Bending is induced by moving the opposite edges of its two ends towards each other, while the bar can rotate freely around these edges. The simulation is performed with the CC model using a constant kernel and a total simulation time of 0.2 s.

The result is shown in Figure 11. The initial configuration with a small curvature is displayed at the top, and the final deformed configuration at the bottom. The bar bends until the two ends nearly touch, resulting in large deformations and rotations. The simulation remains stable and no issues related to zero-energy modes or objectivity are observed.

Both examples confirm that zero-energy modes are not triggered by large deformations. As shown in the previous section, zero-energy modes arise from oscillatory displacement fields, which are fundamentally different from the smooth

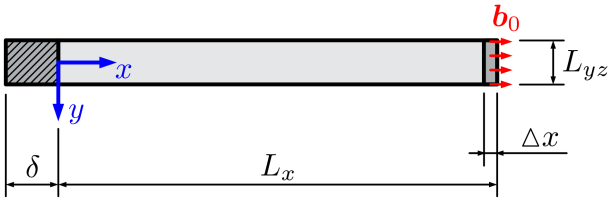

FIGURE 12 Setup of the 3D bar with applied traction load $\boldsymbol{b}_0$.

deformation patterns encountered in the twisting and bending examples. Therefore, the spurious modes observed in static and dynamic settings are triggered by other mechanisms. Since the hyperelastic material laws used here are formulated in terms of the right Cauchy–Green tensor and are therefore objective by construction, the Flanagan & Taylor objectivity enforcement is not required for the examples presented in this work.

5 | NUMERICAL RESULTS

In the following, we present numerical results for the previously introduced peridynamic models. We compare the capabilities regarding modeling elasticity, fracture and crack propagation as well as dynamic fracture and crack branching with simple well known examples. The examples highlight the differences and challenges of the different peridynamic models, which were introduced in Section 3 and Section 4.

5.1 | Tension due to traction loads

In static simulations, the surface effect of incomplete neighborhoods can lead to significant errors in the displacement field when traction loads are applied. Additionally, there is an inherent error in the application of traction loads themselves, since the peridynamic formulation assumes volume forces acting on material points, whereas traction loads are surface forces and the surface is not explicitly represented in peridynamics.

To analyze these errors, a simple 3D bar under traction load is investigated, as illustrated in Figure 12. The bar has a length of $L_x = 100$ mm and a square cross section with side length $L_{yz} = 10$ mm. It is discretized uniformly with a point spacing of $\triangle x = L_{yz}/N_{yz}$, where N_{yz} is the variable number of points across the side length of the cross section. At the left end of the bar, a layer of thickness δ is fixed in all spatial directions. A tensile force of $F_0 = 200$ kN is applied at the right end as a body force $b_0 = F_0/(\triangle x \cdot L_{yz}^2)$ distributed across one layer of material points with thickness $\triangle x$. Because the traction load is applied as a body force, the load is not applied exactly at the surface of the bar, which introduces an error when comparing to a reference solution that assumes the load acts at the surface. This error decreases as $\triangle x \to 0$, but must be accounted for when using traction loads in peridynamic simulations.

To evaluate the simulation results, analytical reference solutions are derived for the length change of the bar. The cross-sectional area is $A = L_{yz}^2$ and the engineering stress is $\sigma_0 = F_0/A$. For linear elasticity assuming small strains, the elongation is

$$\Delta l_{\mathrm{LE}} = \frac{F_0\, L_x}{E\, A}. \tag{5.1}$$

For the Saint Venant–Kirchhoff material, the bar is in a state of uniaxial stress and can deform freely in the transverse directions [18]. In one dimension, the second Piola–Kirchhoff stress is $S = E\, E_{11}$ with the Green–Lagrange strain $E_{11} = (\tilde{\lambda}^2 - 1)/2$, and the engineering stress relates to S through $\sigma_{\mathrm{eng}} = \tilde{\lambda}\, S$. This yields

$$\sigma_0 = \frac{E}{2}\, \tilde{\lambda}\, (\tilde{\lambda}^2 - 1), \tag{5.2}$$

which, after rearranging, leads to the depressed cubic equation

$$\tilde{\lambda}^3 - \tilde{\lambda} - \frac{2\, \sigma_0}{E} = 0. \tag{5.3}$$

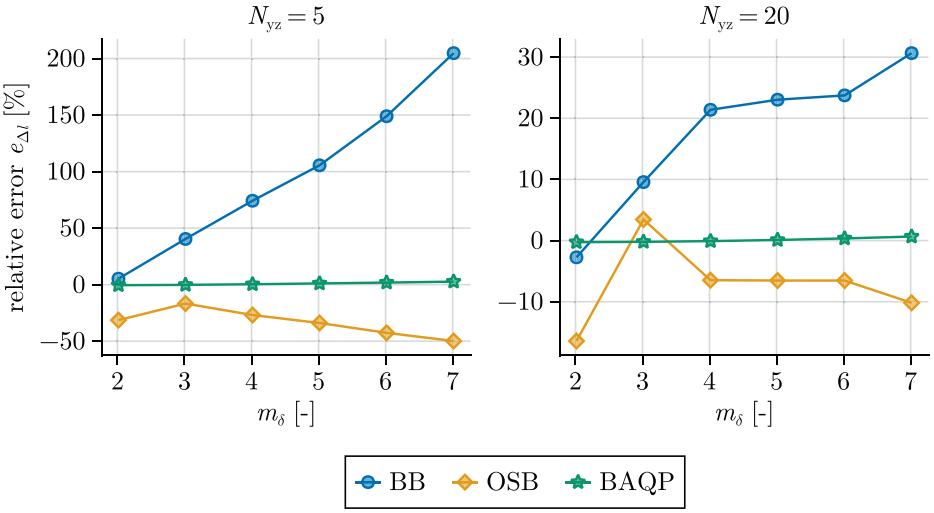

FIGURE 13 Relative errors $e_{\Delta l}$ in length change Δl of the bar as a function of specific horizon ratio $m_\delta = \delta / \triangle x$ for different discretizations, obtained with the JFNK time integration scheme.

This cubic equation is solved analytically using Cardano's formula to obtain the stretch ratio $\tilde{\lambda}$. The elongation for the Sai Venant–Kirchhoff material is then given by

$$\Delta l_{\mathrm{HE}} = (\tilde{\lambda} - 1)\, L_x. \tag{5.4}$$

As in the previous section, the standard formulations compute displacements consistent with the linear elastic solution Δl_{LE}, while the BAQP formulation captures the nonlinear response and is compared against Δl_{HE}.

The relative error in the length change of the bar is defined as

$$e^{\mathrm{LE}}_{\Delta l} = \frac{\overline{\Delta l} - \Delta l_{\mathrm{LE}}}{\Delta l_{\mathrm{LE}}}, \qquad e^{\mathrm{HE}}_{\Delta l} = \frac{\overline{\Delta l} - \Delta l_{\mathrm{HE}}}{\Delta l_{\mathrm{HE}}}, \tag{5.5}$$

where $\overline{\Delta l}$ is the length change of the peridynamic simulation, obtained by averaging the displacement magnitude of the material points at the boundary condition layer at the right end of the bar. For the BB and the OSB model, the reference is the linear elastic solution, that is, $e_{\Delta l} := e^{\mathrm{LE}}_{\Delta l}$ with Δl_{LE} from Equation (5.1). For the CC and BAQP model, the reference is the Saint Venant–Kirchhoff solution, that is, $e_{\Delta l} := e^{\mathrm{HE}}_{\Delta l}$ with Δl_{HE} from Equation (5.4).

In Figure 13, the relative errors $e_{\Delta l}$ in the length change of the bar are shown as a function of the horizon ratio $m_\delta = \delta / \triangle x$ for different discretizations. The results are obtained with the JFNK time integration scheme described in Section 3.8. For a coarse discretization with $N_{yz} = 5$ points across the cross section, the error of the BB model reaches up to around 200% for a horizon ratio of $m_\delta = 7$. Even with a finer discretization of $N_{yz} = 20$ points, the error still reaches around 30% for $m_\delta = 7$. For the OSB formulation, the errors are significantly lower than for the BB model. The BAQP model has errors in the order of 0.3% for all horizon ratios $m_\delta < 4$. For the horizon ratios of $m_\delta = 7$, the error of the BAQP model increases to around 3% for $N_{yz} = 5$ and around 0.6% for $N_{yz} = 20$, which is still significantly lower than the errors of the other formulations.

The main cause for this error in the standard formulations is the surface effect, which leads to a significant deviation of the material response near the surfaces of the bar. However, the error that is observed with the BAQP model is not related to the surface effect, but the inherent error in the application of the traction load. This error is present in all formulations, but for the standard formulations it is overshadowed by the much larger errors from the surface effect. The error from the traction load application decreases with increasing resolution, but increases with increasing horizon ratio. For a horizon ratio of $m_\delta = 3$, it is in the range of 0.2% for all discretizations used with the BAQP model.

In Figure 14, the relative length change errors $e_{\Delta l}$ are shown in relation to the number of points across the cross section N_{yz} for a fixed horizon ratio of $m_\delta = 3$. This shows the reduced stiffness of the material response near the surfaces, which becomes less significant with increasing resolution. The OSB model has lower errors, but converges to a higher error than the BB model. Only the BAQP model again has a constant error of around −0.2% for all discretizations, which is consistent with the error from the traction load application that does not vanish with increasing resolution.

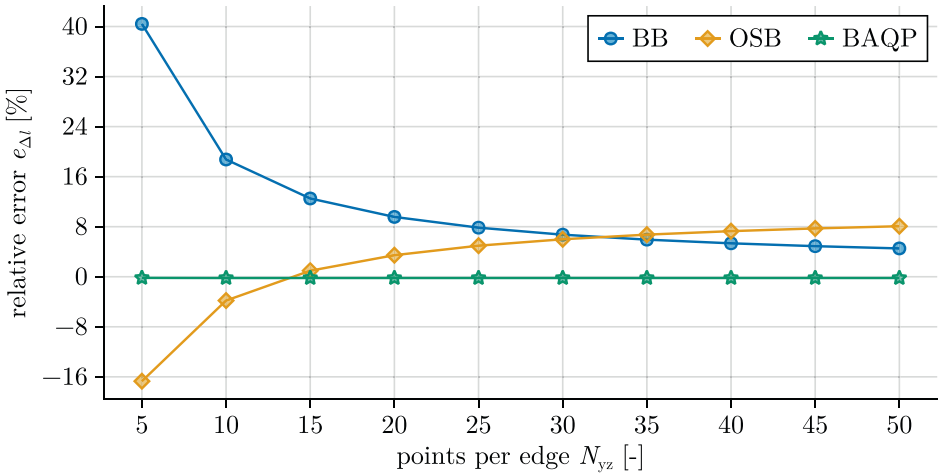

FIGURE 14 Relative errors $e_{\Delta l}$ in length change Δl of the bar as a function of the number of points N_{yz} in the cross section, obtained with the JFNK time integration scheme.

5.2 | Modeling fracture and crack propagation

The most widely used approach to fracture in peridynamics is based on the concept of a critical bond strain. This concept was introduced by Silling and Askari [32] and relies on the idea that a bond between two material points breaks irreversibly once its deformation exceeds a critical threshold. The broken bond then no longer carries any force, effectively modeling the creation of a crack surface. This approach is natural in the peridynamic setting, where the internal forces are defined through bond interactions, and the removal of bonds directly leads to local discontinuities in the displacement field.

The bond strain ε_b defined in Equation (3.10) measures the relative elongation of a bond as

$$\varepsilon_b(t, \boldsymbol{X}, \boldsymbol{X}') = \frac{|\boldsymbol{\Delta x}| - |\boldsymbol{\Delta X}|}{|\boldsymbol{\Delta X}|}.$$

A bond is considered broken when the bond strain exceeds a critical value ε_c, called the *critical bond strain*. To derive ε_c, the Griffith energy criterion [14] is used. The critical energy release rate G_c is related to the energy stored in the bonds and the surface area created by breaking the bonds. This leads to the definition of a failure criterion for the bonds, which can be expressed as

$$\varepsilon_c = \sqrt{\frac{5G_c}{9K\delta}}, \tag{5.6}$$

relating the critical bond strain to the critical energy release rate G_c, the bulk modulus K, and the horizon δ. This result was first derived by Silling and Askari [32] and is widely used in the peridynamics community.

With the critical bond strain defined, individual bonds can be classified as either intact or broken. In a continuous setting, the *bond failure function* $d_b : [0, \infty) \times \mathcal{B}_0 \times \mathcal{B}_0 \to \{0, 1\}$ is defined as

$$d_b(t, \boldsymbol{X}, \boldsymbol{X}') = \begin{cases} 0 & \text{if } \varepsilon_b(t, \boldsymbol{X}, \boldsymbol{X}') > \varepsilon_c, \\ 1 & \text{else.} \end{cases} \tag{5.7}$$

The bond failure is irreversible, meaning that once a bond has failed, it can never heal. A value of $d_b = 0$ indicates a broken bond that carries no force, while $d_b = 1$ indicates an intact bond. To quantify the local amount of damage at a material point, the *point damage* $D : [0, \infty) \times \mathcal{B}_0 \to [0, 1]$ is introduced as

$$D(t, \boldsymbol{X}) = 1 - \frac{\int_{\mathcal{H}(\boldsymbol{X})} d_b(t, \boldsymbol{X}, \boldsymbol{X}') \, \mathrm{d}V'}{\int_{\mathcal{H}(\boldsymbol{X})} \mathrm{d}V'}. \tag{5.8}$$

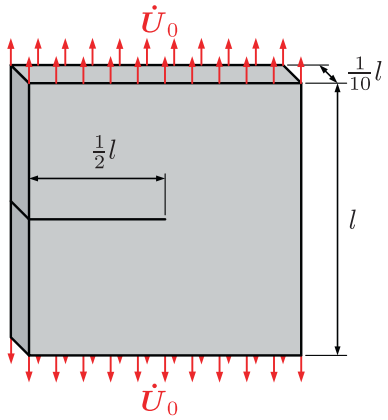

FIGURE 15 Setup for the 3D simulation of a mode I crack in a plate subjected to constant velocity boundary condition at the upper and lower boundary.

The point damage measures the fraction of broken bonds of a point relative to its total number of bonds. A value of $D = 0$ indicates that all bonds are intact, while $D = 1$ indicates that all bonds are broken. A crack surface can be visualized as the set of points with a sufficiently high point damage value, typically $D \geq 0.5$.

To evaluate the performance of different peridynamic formulations in modeling fracture and crack propagation, we simulate a simple mode I crack propagation problem. A plate of the dimensions $l \times l \times 0.1l$ with length $l = 1$ mm is uniformly discretized with $100 \times 100 \times 10$ points and a point spacing of $\vartriangle x = 0.01$ mm. For the simulation, we use a horizon of $\delta = 3.015 \ \vartriangle x$. Linear elastic material parameters are used with a Young's modulus of $E = 210000$ MPa, a Poisson's ratio of $\nu = 0.25$, and a density of $\varrho = 8000$ kg/m^3. The critical energy release rate is set to $G_c = 2.7$ N/mm. We consider a prescribed velocity boundary condition with $\dot{\boldsymbol{U}}_0 = 50$ mm/s on the upper and lower boundary of the geometry, as shown in Figure 15. A predefined crack is introduced from the left side to the center of the plate. This crack is modeled by failing all bonds that cross the crack plane. The modeling of damage and failure is done with a simple critical strain criterion, which is discussed in detail in [12, 27].

In Figure 16, the results of the simulation with different peridynamic formulations are shown. The BB and OSB formulation (see Figure 16A,B) are able to capture the simple crack propagation that is expected for this problem. However, both models use an energy-density based surface correction scheme [22], but still single points with large damage values are visible around the edges of the crack.

The correspondence model with Silling's zero-energy mode stabilization (see Figure 16C,D) demonstrates a strong dependency on the stabilization parameter C_s. With a lower value of $C_s = 10$ (Figure 16C), the crack propagation is not captured but the simulation terminates prematurely due to instabilities. A higher value of $C_s = 100$ (Figure 16D) suppresses the instabilities and allows the simulation to complete successfully. However, the parameter choice depends on the problem and the geometry, and it is not straightforward to find a suitable value that works for all cases.

The correspondence model with Wan's stabilization scheme (see Figure 16E) provides more stable results with a cleaner crack path compared to Silling's approach. Similarly, the bond-associated formulation (Figure 16F) yields a well-defined crack trajectory without the numerical artifacts seen in the other methods. This confirms that both Wan's zero-energy mode stabilization and bond-associated modeling approaches effectively address the instability issues while maintaining accuracy for simple crack propagation modeling.

5.3 | Modeling dynamic fracture and crack branching

To evaluate the performance of different peridynamic formulations in more complex fracture scenarios, we simulate the so-called boundary tension test (BTT). This benchmark is particularly challenging as it involves dynamic crack branching, which can be difficult to capture accurately with certain models. Similar to the setup before, we discretize a plate of the dimensions $l \times \frac{2}{5}l \times \frac{1}{25}l$ with length $l = 100$ mm, uniformly discretized with $200 \times 80 \times 8$ points and a point spacing of $\vartriangle x = 0.5$ mm. For the simulation, we use a horizon of $\delta = 3.015 \ \vartriangle x$. Linear elastic material parameters are used with

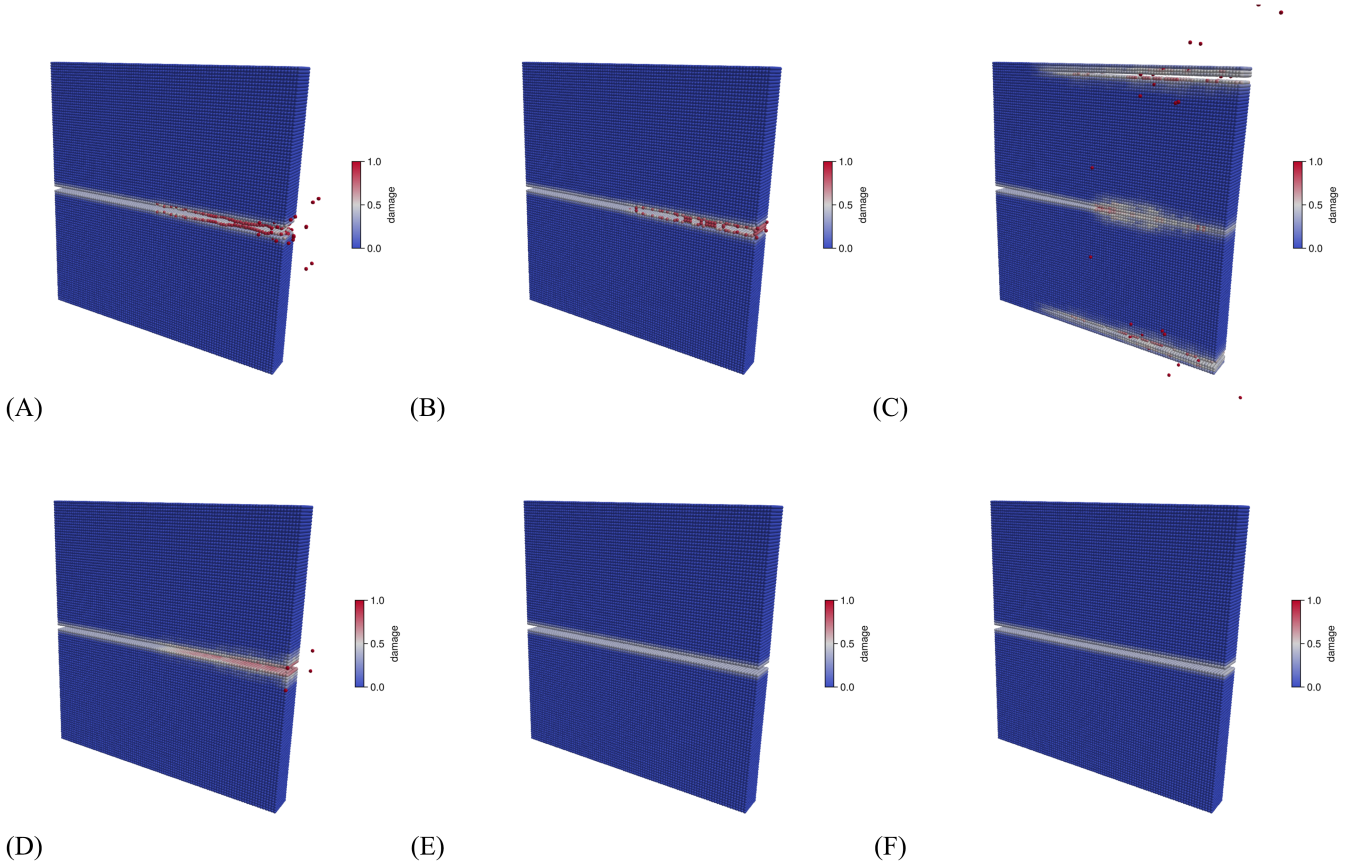

FIGURE 16 Comparison of different peridynamic formulations for mode I crack propagation: (A) BB model, (B) OSB model, the correspondence model using Silling's zero-energy mode stabilization with (C) $C_s = 10$, and (D) $C_s = 100$, (E) the correspondence model with Wan's stabilization scheme, and (F) bond-associated modeling.

a Young's modulus of $E = 32\,000$ MPa, a Poisson's ratio of $\nu = 0.2$, and a density of $\varrho = 2440$ kg/m^3. The critical energy release rate is set to $G_c = 0.75$ N/m. At the upper and lower boundary, a constant dynamic stress field of $\sigma = 1$ MPa is applied. One layer of points in the upper and lower boundary is also defined as a no-failure zone to prevent premature failure at the boundaries. Otherwise, the modeling is similar to the previous example, with a predefined crack introduced from the left side to the center of the plate, as shown in Figure 17.

Figure 18 presents the results obtained with four different peridynamic formulations. The BB formulation (see Figure 18A) captures the expected crack branching pattern, in agreement with experimental observations from the literature and other peridynamic simulations [16]. The OSB formulation (not shown here) captures this pattern in a similar manner. The correspondence model with the Silling stabilization (see Figure 18B) exhibits strong numerical instabilities, resulting in unrealistic damage patterns and premature termination of the simulation. The correspondence model with the Wan stabilization (see Figure 18C) shows improved stability, but fails to reproduce the branching and produces only a single dominant crack path. The BAQP model with the constant kernel function $\omega(\boldsymbol{\Delta X}) = 1$ (see Figure 18D) reproduces the overall branching, but the damage region is visibly broader than the BB result and additional crack splits emerge.

The constant kernel used in Figure 18D does not satisfy the normalization condition $\omega_0(\boldsymbol{X}) = 1$ in Equation (4.34). When the cubic B-spline kernel from Equation (4.35), which does satisfy this condition, is used in the same simulation, the BAQP result changes drastically. Figure 19 shows that the simulation loses stability shortly after the crack reaches the branching point, and the deformation grows uncontrolled.

The deeper cause of both observations is not the kernel choice itself but the degradation of the shape tensor under bond deletion. As bonds break in the vicinity of the crack tip, the family $\mathcal{H}(\boldsymbol{X})$ of each affected material point progressively shrinks and loses its symmetry, and the shape tensor $\boldsymbol{K}$ in Equation (3.31) integrated over this family becomes ill-conditioned. The bond-associated deformation gradient $\tilde{\boldsymbol{F}}$, which is built from $\boldsymbol{K}^{-1}$, then accumulates large errors. We

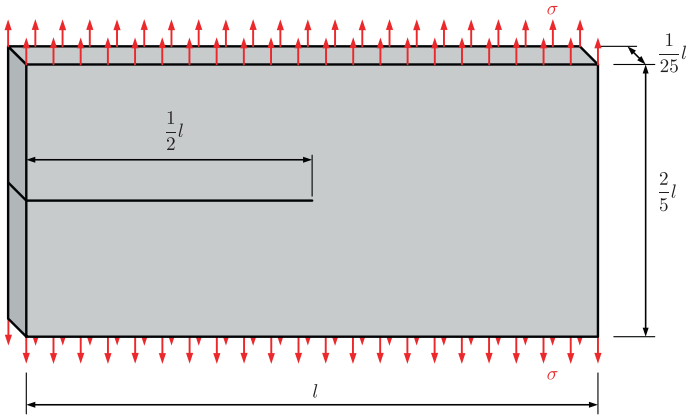

FIGURE 17 Setup for the boundary tension test (BTT) with a pre-notched plate subjected to a dynamic stress field at the upper and lower boundary.

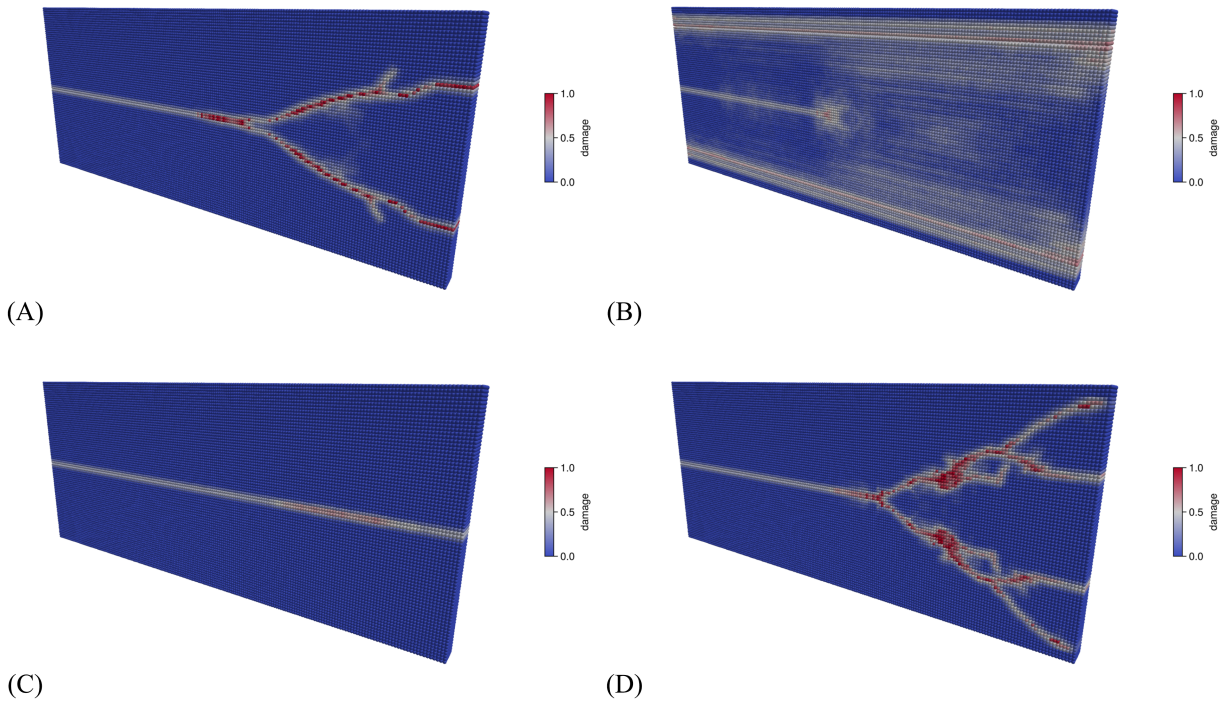

FIGURE 18 Comparison of the different peridynamic formulations for the boundary tension test: (A) BB model, (B) CS model, (C) CW model, and (D) BAQP model with a constant kernel function $\omega(\boldsymbol{\Delta X}) = 1$.

apply a regularization of the shape tensor inverse, which mitigates this effect but does not fully resolve it. The kernel choice controls how the degradation manifests rather than whether it occurs. A constant kernel retains a strong contribution from points far from $\boldsymbol{X}$ and therefore distributes the damage over a broader region with additional crack splits, as visible in Figure 18D. A cubic B-spline kernel concentrates the contributions near $\boldsymbol{X}$, so the shape tensor degrades rapidly once neighboring bonds are deleted and the simulation becomes unstable as in Figure 19. The BB and the OSB formulations do not rely on a shape tensor and are unaffected by this mechanism. The instability is therefore a structural property of the bond-associated quadrature point formulation under progressive bond deletion, not a tuning issue that can be resolved by choosing different parameters or kernels.

The findings of this section can be summarized as follows. The BB and OSB formulations capture both the mode I crack and the dynamic crack branching reliably, although they exhibit a pronounced surface effect that biases elastic results. The correspondence model with the Silling stabilization is sensitive to the choice of C_s and lacks robustness in

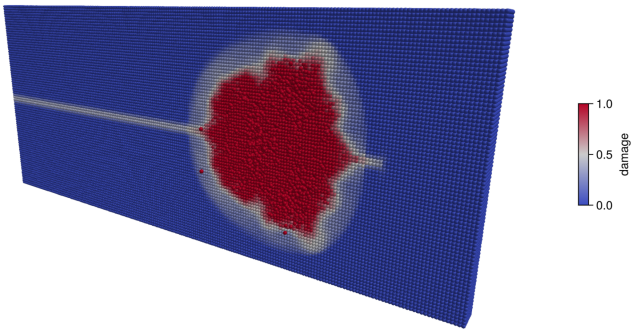

FIGURE 19 Instability of the BAQP model with a cubic kernel function in the boundary tension test simulation.

dynamic fracture. The correspondence model with the Wan stabilization is more stable but inhibits branching. The BAQP formulation, which is the most accurate and stable correspondence-class formulation in the elastic regime as shown in Section 5.1 and in Section 4, loses stability under progressive bond deletion when used with the kernel that the formulation requires. For fracture problems of this kind, the BB and OSB formulations with energy-based surface correction remain the pragmatic choice. A damage formulation in which bond contributions degrade continuously rather than vanishing abruptly may preserve the elastic advantages of the bond-associated quadrature point formulation while keeping the shape tensor sufficiently well-conditioned through fracture, and represents a worthwhile direction for further investigation.

6 | CONCLUSION

In this paper, we have presented a comprehensive analysis of peridynamics as a nonlocal continuum mechanics theory, with particular focus on its theoretical foundations, numerical challenges, and recent advancements in bond-associated modeling approaches. The systematic comparison between classical continuum mechanics and various peridynamic formulations has revealed important insights into their respective strengths and limitations for modeling complex material behavior, especially in the presence of discontinuities.

Our theoretical analysis established the mathematical connections between local and nonlocal continuum theories, providing a deeper understanding of how peridynamics generalizes classical concepts to accommodate material discontinuities. The fundamental difference lies in the replacement of stress tensors with nonlocal force interactions through material bonds, which naturally allows for the modeling of crack initiation and propagation without special numerical treatments.

The numerical investigations demonstrated that while the standard peridynamics formulations can effectively capture crack propagation, they exhibit characteristic surface effects near boundaries. The correspondence formulation overcomes the inherent limitations of the BB approach, such as the fixed Poisson's ratio, but introduce numerical instabilities in the form of zero-energy modes. Our results clearly illustrated that current zero-energy mode stabilization techniques are still not fully effective, lacking robustness for complex fracture scenarios. The penalty stabilizations of Silling and of Wan suppress unstable growth in dynamic settings through additional forces, but they do not modify the approximated deformation gradient and therefore do not register any prescribed checkerboard deformation. The bond-associated quadrature point construction is the only correspondence-class formulation in this study that captures this deformation correctly.

For smooth large deformations, hyperelastic constitutive models formulated in terms of the right Cauchy–Green tensor remain stable without explicit objectivity enforcement. Both the twisting bar and the bending bar simulations in Section 4 stay stable throughout the deformation history. The Flanagan and Taylor algorithm and similar incremental rotation schemes are therefore not required when an objective hyperelastic strain measure is used, which narrows the practical relevance of these enforcement techniques in the context studied here.

The traction-load study in Section 5 confirms the elastic strengths of the bond-associated quadrature point formulation. The bond-based and the ordinary state-based formulations exhibit a pronounced surface effect that grows with the horizon ratio and is reduced only slowly by refinement. The bond-associated quadrature point formulation, in contrast, maintains errors below one percent across all discretizations and horizon ratios considered. In the elastic regime, this formulation is the most accurate and stable correspondence-class formulation among those compared.

The picture changes once bonds are allowed to break. In the dynamic crack branching benchmark, the bond-associated quadrature point formulation loses stability for certain kernel function choices. Progressive bond deletion shrinks and asymmetrizes the family of each material point, and the shape tensor on which the bond-associated deformation gradient relies becomes increasingly ill-conditioned. The bond-based and the ordinary state-based formulations do not invert a shape tensor and remain robust through branching. For fracture problems with substantial bond deletion, the bond-based and the ordinary state-based formulation with energy-based surface correction therefore remain the pragmatic choice.

This observation suggests a direction for further investigation. A damage formulation in which bond contributions degrade continuously rather than vanishing abruptly may preserve the elasticity advantages of the bond-associated quadrature point formulation while leaving the shape tensor sufficiently well-conditioned to integrate the bond-associated deformation gradient through fracture.

ACKNOWLEDGEMENTS

The authors gratefully acknowledge the support of the Deutsche Forschungsgemeinschaft (DFG) in the project WE 2525/15-1 and WE 2525/15-2 within the Special Priority Program 2256 "Variational Methods for Predicting Complex Phenomena in Engineering Structures and Materials" #422730790. Open Access funding enabled and organized by Projekt DEAL.

CONFLICT OF INTEREST STATEMENT

The authors declare no conflicts of interest.

FUNDING INFORMATION

This work was supported by Deutsche Forschungsgemeinschaft (422730790).

DATA AVAILABILITY STATEMENT

The data that support the findings of this study are available from the corresponding author upon reasonable request.

ORCID

Kai Partmann https://orcid.org/0000-0002-5238-4355
Christian Wieners https://orcid.org/0000-0001-6242-6777

REFERENCES

[1] Y. Bazilevs, M. Behzadinasab, and J. T. Foster, Simulating concrete failure using the microplane (M7) constitutive model in correspondence-based peridynamics: Validation for classical fracture tests and extension to discrete fracture, J. Mech. Phys. Solids **166** (2022), 104947.
[2] M. Behzadinasab, J. T. Foster, and Y. Bazilevs, A unified, stable and accurate meshfree framework for peridynamic correspondence modeling—Part II: Wave propagation and enforcement of stress boundary conditions, J. Peridyn. Nonlocal Model. **3** (2021), no. 1, 46–66.
[3] M. Behzadinasab, N. Trask, and Y. Bazilevs, A unified, stable and accurate meshfree framework for peridynamic correspondence modeling—Part I: Core methods, J. Peridyn. Nonlocal Model. **3** (2021), 1–22.
[4] T. Belytschko, J. S. J. Ong, W. K. Liu, and J. M. Kennedy, Hourglass control in linear and nonlinear problems, Comput. Methods Appl. Mech. Eng. **43** (1984), no. 3, 251–276.
[5] M. A. Bessa, J. T. Foster, T. Belytschko, and W. K. Liu, A meshfree unification: Reproducing kernel peridynamics, Comput. Mech. **53** (2014), no. 6, 1251–1264.
[6] W. Chan and H. Chen, Peridynamic bond-associated correspondence model: Reformulation and comparison study, Int. J. Numer. Methods Eng. **123** (2022), no. 20, 4957–4973.
[7] H. Chen, Bond-associated deformation gradients for peridynamic correspondence model, Mech. Res. Commun. **90** (2018), 34–41.
[8] H. Chen and B. W. Spencer, Peridynamic bond-associated correspondence model: Stability and convergence properties, Int. J. Numer. Methods Eng. **117** (2019), no. 6, 713–727.
[9] D. Flanagan and L. Taylor, An accurate numerical algorithm for stress integration with finite rotations, Comput. Methods Appl. Mech. Eng. **62** (1987), no. 3, 305–320.
[10] D. P. Flanagan and T. Belytschko, A uniform strain hexahedron and quadrilateral with orthogonal hourglass control, Int. J. Numer. Methods Eng. **17** (1981), no. 5, 679–706.
[11] K. Friebertshäuser (Partmann), C. Wieners, and K. Weinberg, Dynamic fracture with continuum-kinematics-based peridynamics, AIMS Mater. Sci. **9** (2022), no. 6, 791–807.

[12] K. Friebertshäuser, M. Werner, and K. Weinberg, Pneumatic fracture computations with peridynamics, Proc. Struct. Integrity **35** (2022), 159–167 2nd International Workshop on Plasticity, Damage and Fracture of Engineering Materials (IWPDF 2021), 18–20 August 2021, Ankara, Turkey.
[13] G. Ganzenmüller, S. Hiermaier, and M. May, On the similarity of meshless discretizations of peridynamics and smooth-particle hydrodynamics, Comput. Struct. **150** (2015), 71–78.
[14] A. A. Griffith, Vi. The phenomena of rupture and flow in solids, Philos. Trans. R. Soc. Lond. Ser. A Math. Phys. Eng. Sci. **221** (1921), no. 582–593, 163–198.
[15] H. Grubmüller, H. Heller, A. Windemuth, and K. Schulten, Generalized Verlet algorithm for efficient molecular dynamics simulations with long-range interactions, Mol. Simul. **6** (1991), 121–142.
[16] Y. D. Ha and F. Bobaru, Studies of dynamic crack propagation and crack branching with peridynamics, Int. J. Fract. **162** (2010), no. 1–2, 229–244.
[17] M. Hillman, M. Pasetto, and G. Zhou, Generalized reproducing kernel peridynamics: Unification of local and non-local meshfree methods, non-local derivative operations, and an arbitrary-order state-based peridynamic formulation, Comput. Part. Mech. **7** (2020), no. 2, 435–469.
[18] G. A. Holzapfel, Nonlinear solid mechanics: A continuum approach for engineering science, Meccanica **37** (2002), no. 4/5, 489–490.
[19] A. Javili, S. Firooz, A. T. McBride, and P. Steinmann, The computational framework for continuum-kinematics-inspired peridynamics, Comput. Mech. **66** (2020), no. 4, 795–824.
[20] A. Javili, A. McBride, and P. Steinmann, Continuum-kinematics-inspired peridynamics. Mechanical problems, J. Mech. Phys. Solids **131** (2019), 125–146.
[21] D. A. Knoll and D. E. Keyes, Jacobian-free newton–Krylov methods: A survey of approaches and applications, J. Comput. Phys. **193** (2004), no. 2, 357–397.
[22] Q. V. Le and F. Bobaru, Surface corrections for peridynamic models in elasticity and fracture, Comput. Mech. **61** (2018), no. 4, 499–518.
[23] D. J. Littlewood, *Roadmap for peridynamic software implementation, Technical report*, Sandia National Laboratories, Albuquerque, NM, 2015.
[24] W. K. Liu, S. Jun, and Y. F. Zhang, Reproducing kernel particle methods, Int. J. Numer. Methods Fluids **20** (1995), no. 8–9, 1081–1106.
[25] E. Madenci and E. Oterkus, *Peridynamic theory and its applications*, Springer, New York, 2014.
[26] K. Partmann, M. Dienst, and K. Weinberg, Peridynamic computations of wave propagation and reflection at material interfaces, Arch. Appl. Mech. **94** (2024), 2405–2416.
[27] K. Partmann, C. Wieners, and K. Weinberg, Continuum-kinematics-based peridynamics and phase-field approximation of non-local dynamic fracture, Int. J. Fract. **244** (2023), no. 1–2, 187–200.
[28] S. Reese and P. Wriggers, A stabilization technique to avoid hourglassing in finite elasticity, Int. J. Numer. Methods Eng. **48** (2000), no. 1, 79–109.
[29] Y. Saad and M. H. Schultz, Gmres: A generalized minimal residual algorithm for solving nonsymmetric linear systems, SIAM J. Sci. Stat. Comput. **7** (1986), no. 3, 856–869.
[30] P. Seleson and M. Parks, On the role of the influence function in the peridynamic theory, Int. J. Multisc. Comput. Eng. **9** (2011), no. 6, 689–706.
[31] S. Silling, Stability of peridynamic correspondence material models and their particle discretizations, Comput. Methods Appl. Mech. Eng. **322** (2017), 42–57.
[32] S. Silling and E. Askari, A meshfree method based on the peridynamic model of solid mechanics, Comput. Struct. **83** (2005), no. 17–18, 1526–1535.
[33] S. A. Silling, Reformulation of elasticity theory for discontinuities and long-range forces, J. Mech. Phys. Solids **48** (2000), no. 1, 175–209.
[34] S. A. Silling. Peridynamic modeling of the Kalthoff-Winkler experiment. Submission for the 2001 Sandia Prize in Computational Science 2002.
[35] S. A. Silling, M. Epton, O. Weckner, J. Xu, and E. Askari, Peridynamic states and constitutive modeling, J. Elast. **88** (2007), no. 2, 151–184.
[36] J. Trageser and P. Seleson, Bond-based peridynamics: A tale of two Poisson's ratios, J. Peridyn. Nonlocal Model. **2** (2020), no. 3, 278–288.
[37] C. Truesdell and W. Noll, *The non-linear field theories of mechanics*, 3rd ed., Springer, Berlin, Heidelberg, 2004.
[38] L. Verlet, Computer experiments on classical fluids. I. Thermodynamical properties of Lennard-Jones molecules, Phys. Rev. **159** (1967), 98–103.
[39] J. Wan, Z. Chen, X. Chu, and H. Liu, Improved method for zero-energy mode suppression in peridynamic correspondence model, Acta Mech. Sinica **35** (2019), no. 5, 1021–1032.
[40] J. Wang, M. Behzadinasab, W. Li, and Y. Bazilevs, A stable formulation of correspondence-based peridynamics with a computational structure of a method using nodal integration, Int. J. Numer. Methods Eng. **125** (2024), no. 11, e7465.

How to cite this article: K. Partmann, R. I. Weinbrenner, C. Wieners, and K. Weinberg, *Local continuum consistent peridynamics with bond-associated modeling and dynamic fracture*, GAMM-Mitteilungen. **49** (2026), e70014. https://doi.org/10.1002/gamm.70014